UNIVERSITY OF OKLAHOMA

GRADUATE COLLEGE

INTEGRATED SYSTEM TO REDUCE EMISSIONS FROM A NATURAL GAS-FIRED RECIPROCATING ENGINE

A THESIS

SUBMITTED TO THE GRADUATE FACULTY

in partial fulfillment of the requirements for the

Degree of

MASTER OF SCIENCE

By

HAFIZ AHMAD HASSAN

Norman, Oklahoma

2022

INTEGRATED SYSTEM TO REDUCE EMISSIONS FROM A NATURAL GAS-FIRED RECIPROCATING ENGINE

A THESIS APPROVED FOR THE

SCHOOL OF AEROSPACE AND MECHANICAL ENGINEERING

BY THE COMMITTEE CONSISTING OF

Dr. Pejman Kazempoor**,** Chair

Dr. Ramkumar N. Parthasarathy

Dr. Hamidreza Shabgard

Acknowledgments

Firstly, I would like to express my gratitude to my advisor Dr. Pejman Kazempoor for providing me with an opportunity to research emission reduction. Moreover, I am thankful for his guidance and support throughout this journey for my research and career as a whole.

Secondly, I would like to thank the committee members Dr. Ramkumar N. Parthasarathy and Dr. Hamidreza Shabgard for their valuable time serving on my thesis committee.

Thirdly, I would like to thank my parents for their continuous support, which has been the backbone of my career.

Lastly, I thank all my team members at the Natural Gas Lab of the University of Oklahoma. Working with a diverse group of people has been a great learning experience. I hope you all keep working hard and succeed in your goals! The individual contributions of each member in this thesis include Matthew D. Hartless (Figures 25-28); Tu Nguyen, Matthew D. Hartless, Mohammed A. Moinuddin Ansari, and Raelin B. Lane (Data collection for experiments); James D. Lynch (Pictures of lab setup); Scott Rosser and James D. Lynch (setting up the experiments).

Table of Contents

Abbreviations

AFR	Air-to-Fuel Ratio
AMP	Air Management Package
CA	Crank Angle
CCV	Cycle-to-Cycle Variability
CH_4	Methane
CO	Carbon Monoxide
CO_2	Carbon Dioxide
EES	Engineering Equation Solver
EGR	Exhaust Gas Recirculation
EPA	Environmental Protection Agency
FTIR	Fourier Transform Infrared Spectroscopy
HMI	Human-Machine Interface
HRR	Heat Release Rate
IC	Internal Combustion
IMEP	Indicated Mean Effective Pressure
ITE	Indicated Thermal Efficiency
LPG	Liquified Petrolium Gas
LPM	Liters Per Minute
N_2	Nitrogen
NGFRE	Natural Gas-Fired Reciprocating Engines
NOx	Nitrogen Oxides
O_2	Oxygen
PCC	Pre-Combustion Chamber
PLC	Programmable Logic Controller
PM	Particulate Matter
SHE	Standard Hydrogen Electrode

SI	Spark Ignition
TDC	Top Dead Center
VOCs	Volatile Organic Compounds
$\sigma_{P_{peak}}$	Standard Deviation Of Peak Pressure

List of Figures

List of Tables

Abstract

Internal Combustion (IC) engines are a significant source of environmental pollution; therefore, global efforts are being made for their growth and sustainability. Mainly, the Natural Gas-Fired Reciprocating Engines (NGFRE), which are naturally aspirated, exhibit increased combustion instability and higher emissions, predominantly methane (CH_4) and Volatile Organic Compounds (VOCs) at lower loads, resulting in restrictions on the operational envelope of such engines. This thesis reviews some of the emission reduction technologies for NGFREs and presents the experimental investigation of an integrated system to reduce emissions and improve the combustion performance of an NGFRE. The integrated system consists of an air management package and integrated sensors including an amperometric NOx/O_2 sensor, exhaust temperature thermocouple, pressure transducers and vibration sensors. A comprehensive electrochemical model for the NOx/O_2 sensor is developed to quantitatively analyze the degradation of the sensor's electrode material under a harsh two-stroke engine exhaust environment. The NGFRE under study is a naturally aspirated, stationary, lean-burn engine and is used in the oil and gas industry for the production, storage, processing and transmission of natural gas extracted from wells. Experiments were carried out using natural gas and natural gas/propane blends at different load steps, and combustion performance, as well as the emissions, were analyzed. For natural gas fuel, the results show that the standard deviation of peak pressure and indicated thermal efficiency (ITE) improved by 67.4 psi and 4.2% respectively, at 40% load. Similarly, CH_4 and Nitrogen Oxides (NOx) emissions reduced considerably by 84% and 63% respectively, whereas an abrupt behavior in Carbon Monoxide (CO) and NOx emissions was observed. At 60% load, the ITE improved by 3.8% and the CH_4 emissions were reduced by 68%. The reduction in VOCs emissions was 63% at 40% load and 69% at 60% load. The findings of this research provide evidence

of the effectiveness of the integrated system in improving the sustainability of NGFREs. In general, this technology can be implemented on air-assisted combustion applications to improve combustion performance and, consequently, reduce emissions. The next step in the research is to develop a data analytics model using machine learning techniques to predict the optimum operation of the integrated system at different loads. The test procedure and data analysis techniques described in this thesis will be used in other research tasks, such as obtaining the training data for the machine learning model and investigating natural gas/hydrogen blends as fuel.

Chapter 1

Introduction

This section describes the problem statement in detail and explains the process of emission formation in the engines and a general approach to reducing each emission type. Moreover, the thesis layout is also presented briefly at the end.

1.1 Background

As the human population grows and the standard of living improves, the global energy demand and fossil fuel consumption increase. Because of their higher power-to-weight ratio than battery and fuel cell-operated engines, the IC engines are supposed to be dominant for another century (Aslam, Masjuki et al. 2006). Still, improved designs and alternative fuels are inevitable for better thermal efficiency and lesser pollutant emissions (Korakianitis, Namasivayam et al. 2011). In terms of sustainability, natural gas is considered to be an excellent alternative to gasoline as it produces less CO, CO_2, and VOCs emissions and is available in abundance (Karim, Wierzba et al. 1996, Wang, Huang et al. 2007) (Ma, Wang et al. 2007). Natural gas mainly consists of CH_4 with smaller percentages of higher hydrocarbons such as ethane, propane, and sometimes CO_2, Nitrogen (N_2), and He depending on the climate, location, or processing of the gas (Kojima, Brandon et al. 2000, Chen, He et al. 2019). Besides its ability to produce fewer emissions, natural gas engines have higher compression ratios and higher knock resistance than gasoline (Wang, Huang et al. 2007, Korakianitis, Namasivayam et al. 2011, Sevik, Pamminger et al. 2016, Chen, He et al. 2019). However, the natural gas engines produce lower power than gasoline engines and have higher combustion instability in lean-burn conditions (Wang, Huang et al. 2007). Despite these drawbacks, there is an increasing trend in the production and usage of natural gas

(da Costa, Hernandez et al. 2019). Figure 1 shows the historical natural gas withdrawal in the USA from 1980 to 2022.

The engine under study is a lean-burn two-stroke engine coupled with a reciprocating compressor. The application of these integral engine-compressor units ranges from production, gathering, transportation and processing sections of the natural gas industry. Currently, there are more than 7,500 such units in North America. Due to fluctuating demands in the natural gas supply, these engines must run at part loads occasionally, resulting in bad combustion performance and higher emissions as they are designed to run optimally at only their rated loads. Consequently, these units must be replaced with ones having lower rated load. To avoid this situation, an integrated system consisting of an air management package, integrated sensors and a human-machine interface (HMI) is presented by (Gubba, Tamma et al. 2021) (Hassan, Hartless et al. 2022). This system is explained in detail later.

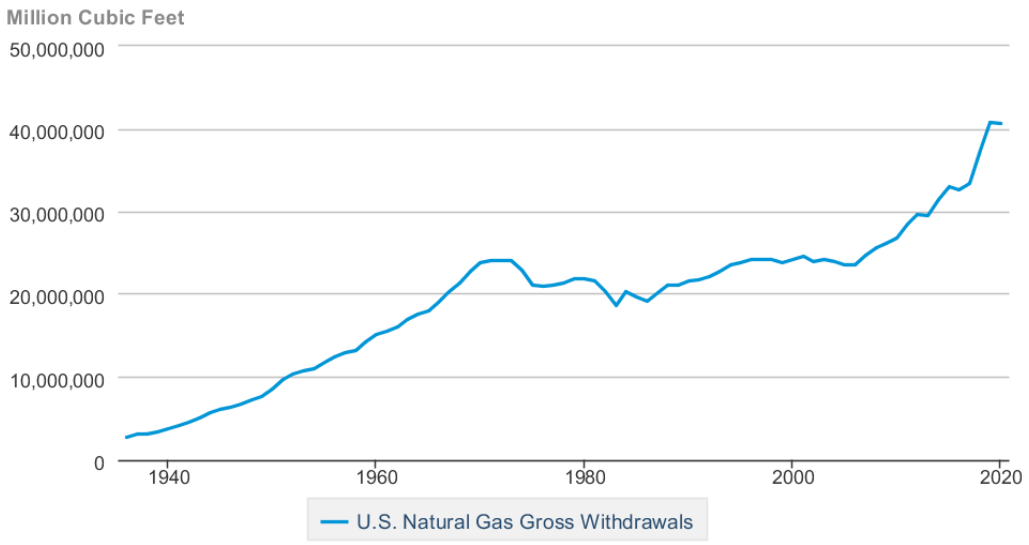

Figure 1. US Natural Gas Gross Withdrawals [www.eia.gov]

Two-stroke engines are well known for their greater power output, simplicity, and compactness compared to four-stroke engines, but the emissions and fuel consumption are higher (Ishibashi and Asai 1996). The Environment Protection Agency's (EPA) "New Source Performance Standards" include stringent emissions monitoring such as NOx, VOCs, CH_4, and CO from NGFREs (2021, Gubba, Tamma et al. 2021, Hassan, Hartless et al. 2022). One of the most significant drawbacks of using natural gas fuel is the higher CH_4 emissions which have 25-34 times more global warming potential than CO_2 over 100 years (Korakianitis, Namasivayam et al. 2011, Yang, Yang et al. 2018) (Cooper, Balcombe et al. 2021). Moreover, in two-stroke engines, the percentage of unburned fuel is greater than in four-stroke engines because of the design of ports and subsequent scavenging losses (Kojima, Brandon et al. 2000). Therefore, the CH_4 emissions from a two-stroke NGFRE are high, and it is essential to decrease them and improve the sustainability of such NGFREs. Furthermore, under part-load conditions, natural gas combustion faces instability issues (Wang, Huang et al. 2007) (Sevik, Pamminger et al. 2016).

Lean combustion technology is useful in producing low emissions such as NOx and has better thermal efficiency and lower knock (Karim, Wierzba et al. 1996). However, at part load conditions, the decreased exhaust gas temperatures tend to reduce the catalytic activity of the catalyst, and the combustion stability declines as well (Karim, Wierzba et al. 1996). Moreover, at lower loads, the fueling is reduced to decrease the brake horsepower, but the air intake flow rate remains the same as it depends on the RPMs. This higher air intake leads to very high air-to-fuel ratios (AFRs), which exacerbate combustion stability and emissions.

1.2 Emissions Formation and Hazards

NOx, CO, CH_4 and VOCs have harmful effects on human health and the atmosphere, and it is necessary to reduce their inclusion in the environment (Hassan, Hartless et al. 2022).

1.2.1 NOx

NOx emissions refer to oxides of nitrogen, including NO, NO_2, and N_2O. Most of the NOx emissions produced during combustion are NO, then NO_2, and at the end, N_2O. There are three types of NOx emissions that are formed in an engine. Thermal NOx emissions are formed by the reaction of nitrogen with oxygen in air present inside the combustion chamber because of the high temperature as of the extended Zeldovich mechanism (Aslam, Masjuki et al. 2006) (Heywood 2018) (Baukal Jr 2012) (Toof 1986) (Chapman and Nuss-Warren 2007).

$$N_2+O \rightarrow NO+N \quad (1)$$

$$N+O_2 \rightarrow NO+O \quad (2)$$

$$N+OH \rightarrow NO+H \quad (3)$$

Prompt NOx emissions are related to the reactions at the flame front and are time dependent. The prompt NOx emissions are a result of fast reactions of hydrocarbons with atmospheric nitrogen and oxygen (Baukal Jr 2012). Fuel NOx emissions are formed by the reaction of atmospheric oxygen with the nitrogen present in fuel (Chapman and Nuss-Warren 2007). NOx emissions are responsible for harmful environmental effects such as acid rain, severe health issues, and smog. In sunlight, NOx and VOCs form Ozone in the lower atmosphere, which is a severe health hazard (Baukal Jr 2012, Heywood 2018, Hassan, Hartless et al. 2022). The only considerable NOx emissions generated in the NGFRE are thermal NOx (Gubba,

Tamma et al. 2021). Therefore, the best strategy to control NOx emissions is to reduce the combustion temperature.

1.2.2 CO

CO is a colorless and odorless gas that, when breathed, deprives the human body of oxygen and leads to unconsciousness and suffocation (Hassan, Hartless et al. 2022). CO emissions are generally caused by incomplete combustion or partial burning. Incomplete combustion usually happens due to insufficient oxygen or combustion temperature required to convert the carbon atoms in the fuel to CO_2 (Chapman and Nuss-Warren 2007) (Sekar, Praveenkumar et al. 2021) (Ren, Lou et al. 2021). 22% of the total CO emissions are produced by non-road vehicles and engines such as the one being studied (Dey and Dhal 2019).

1.2.3 VOCs

VOCs, also referred to as non-methane non-ethane hydrocarbons, are formed by the presence of higher hydrocarbons such as propane in the fuel gas. VOCs form in the exhaust gas if these higher hydrocarbons are not burned or incompletely burned during the combustion process (Chapman and Nuss-Warren 2007) (Ren, Lou et al. 2021). VOCs can deplete the Ozone layer in the stratosphere, which prevents harmful ultraviolet rays from entering the Earth (Baukal Jr 2012, Hassan, Hartless et al. 2022). VOCs are not significant for natural gas fuels with a lower percentage of higher hydrocarbons. Nevertheless, a larger concentration of these higher hydrocarbons can lead to a dramatic increase in VOCs.

1.2.4 CH_4

CH_4 is the unburned fuel that goes through the combustion chamber without burning and moves to the exhaust. Other causes of CH_4 formation are lower oxygen

in the combustion chamber as well as lower combustion temperatures. In the US, 30% of CH_4 emissions are produced by the natural gas and petroleum systems.

Other emissions such as SOx and particulate matter (PM) are not of considerable significance for natural gas-fired engines as SOx depend on the sulfur content of the fuel, which is very low in natural gas fuels whereas, PM emissions are a concern for engines with liquid fuels (Chapman and Nuss-Warren 2007).

Table 1 shows the emission standards set by EPA for a stationary NGFRE (Hassan, Hartless et al. 2022) (Gubba, Tamma et al. 2021) (2021).

1.3 Thesis Structure

The thesis is divided into three parts. Chapter 2 presents a literature review of emission reduction technologies and their effect on combustion performance for reciprocating engines. Moreover, the integrated system is explained in detail and objectives of the research are delineated. In chapter 3, the methods and procedures are explained for the integrated system with the experimental setup. Results from testing of the air management package are discussed in chapter 4. Moreover, the electrochemical model for the amperometric NOx/O_2 sensor is developed and its working and behavior are thoroughly explained in chapter 5. Whereas chapter 6 presents the conclusion to this study and sheds light on the future proceedings at the Natural Gas Lab of the University of Oklahoma.

Table 1. NOx, CO, and VOCs emission standards for stationary Spark Ignition (SI) engines

Engine type and fuel	**Maximum engine power**	**Manufacture date**	**Emission standard**		
			ppmvd at 15% O_2		
			NOx	**CO**	**VOCs**
Non-emergency natural gas and non-emergency SI lean burn LPG	100 ≤ HP < 500	7/1/2008	160	540	86
		1/1/2011	82	270	60
Non-emergency SI lean 500 ≤ HP < 1350 burn natural gas and LPG	500 ≤ HP < 1350	1/1/2008	160	540	86
		7/1/2010	82	270	60
Non-emergency SI natural gas and non-emergency SI lean burn LPG (except lean burn 500 ≥ HP < 1350) Landfill/digester (except lean burn 500 ≥ HP < 1350)	HP ≥ 500	7/1/2007	160	540	86
	HP ≥ 500	7/1/2010	82	270	60
	HP < 500	7/1/2008	220	610	80
		7/1/2011	150	610	80
	HP ≥ 500	7/1/2007	220	610	80
		1/1/2010	150	610	80
Landfill/digester gas lean burn	500 ≥ HP < 1350	7/1/2008	220	610	80
Emergency	25 ≥ HP < 130	1/1/2009	150	610	80
	HP ≥ 1300		N/A	N/A	N/A
			160	540	86

ppmvd: parts per million, volumetric dry; LPG: liquefied petroleum gas.

Chapter 2

2.1 Literature Review

In this section, some of the emission reduction technologies for reciprocating engines are reviewed and their feasibility in terms of the test engine is discussed. Moreover, the integrated system is explained in detail.

There are two types of emission reduction methods in reciprocating engines. Pre-combustion methods are those where the emissions are reduced by changing the combustion parameters. Post-combustion methods are those where the exhaust gases are treated separately after the combustion has occurred. An explanation of different methods and their feasibility for the test engine is given below.

2.1.1 Exhaust Gas Recirculation

Exhaust gas recirculation (EGR) is a method where a portion of the exhaust gas is brought back to the combustion zone through the incoming air. This method is effective because most flue gases are inert and have higher heating capacities, such as N_2 and H_2O. When brought back to the combustion zone, these gases help dilute the air/fuel mixture and absorb more heat from combustion, reducing thermal NOx (Keith Hohn 2011). The temperature increases less than typical lean combustion for an equal amount of energy released into the cylinder. EGR also helps reduce the flame speed at higher loads, resulting in lower NOx (Hillier and Coombes 2004). (Jeeragal and Subramanian 2019) performed 0-28% EGR on a hydrogen-fueled SI engine run at 1.4 kW (i.e., 50% of the rated power) and found out that the thermal effect of exhaust gases is not that significant till 20% EGR. However, this effect gets significant at higher percentages because of higher water vapor content in recirculated exhaust gases. At 28% EGR, the NOx emissions went down to 5.3 g/kWh from 12.4 g/kWh at no EGR. As EGR serves to reduce the combustion

temperature, it is useful to be employed with other advanced technologies (Wei, Zhu et al. 2012). EGR can be further classified into two types, i.e., cooled EGR and hot EGR. In cooled EGR, the exhaust gases are cooled down before mixing with the intake air. This further decreases the combustion temperature and hence the NOx emissions also decrease. Moreover, it increases the volumetric efficiency as the density of the incoming air increases. The drawbacks of cooled EGR are that it increases the combustion variability and hydrocarbon emissions compared to hot EGR. In hot EGR, the exhaust gases are mixed with the intake air without cooling down. Hot EGR causes the engine's combustion performance to increase but increases thermal NOx. Hot EGR also decreases hydrocarbon and CO emissions (Wei, Zhu et al. 2012). Another way to classify EGR is internal and external EGR. In internal EGR, the exhaust gases are restricted by varying the exhaust pipe diameter. In external EGR, the exhaust gases are brought into the intake from the exhaust using a piping system. (Andwari, Aziz et al. 2017) applied the internal and external hot-EGR, in ranges 10-20% and 4-12% respectively, on a naturally aspirated, single cylinder, two-stroke, SI engine at 1000, 1500 and 2000 RPMs and found that the VOCs and CO decreased, but NOx increased. This technology is still under development for natural-gas-burning engines, and as significant changes are required to the air intake and exhaust systems, this technology is ineffective in terms of cost (Keith Hohn 2011).

2.1.2 Turbocharger

Compressing the intake air through a turbocharger effectively increases the AFR and reduces the in-cylinder temperature, leading to lower thermal NOx. A lean-burn engine produces better fuel economy and lower carbon-based emissions (Hillier and Coombes 2004). A drawback of lean-burn combustion is the increased combustion instability (Chen, He et al. 2019). Generally, a turbocharger is used to compress the air before entering the cylinder and increases air mass per cycle. This

way, the AFR can be made leaner. A turbocharger can achieve a significant reduction in NOx (up to 90%) and a better fuel economy. However, the cost is very high as an intercooler for compressed air and changes to the ignition system are required (Keith Hohn 2011).

2.1.3 Spark Retardation

In SI engines, the spark is set to ignite the air/fuel mixture when the piston reaches a specific position. This ignition timing can be modified. Ignition timing greatly influences the engine performance parameters such as in-cylinder pressure and temperature (Ma, Li et al. 2012). As the timing is changed, the in-cylinder temperature also varies. This variation in temperature leads to a change in concentrations of thermal NOx (Hillier and Coombes 2004, Gao, Tian et al. 2021). Advancing the spark timing increases the NOx emissions and retarding the spark timing reduces the NOx emissions (Heywood 2018). (Jeeragal and Subramanian 2019) applied the spark timing technique on a single-cylinder hydrogen-fueled SI engine and found out that spark retardation at about 4^{o}CA from a base spark timing of 20^{o}CA before top dead center (TDC) leads to NOx reduction of up to 33%. However, the tradeoff is a reduction of 17% in brake thermal efficiency (Jeeragal and Subramanian 2019) (Keith Hohn 2011). It is a low-cost technique and relatively easier to implement. However, this technology does not provide access to changing the combustion parameters while the engine is in running condition.

2.1.4 Variable Valve Timing

Variable valve timing involves changing the duration of valve overlap that causes the combustion temperature to reduce because of the presence of some residual exhaust gases during the compression stroke. This technology causes lower thermal

NOx (Hillier and Coombes 2004). However, it cannot be applied to the engine being studied as it is not operated by valves.

2.1.5 Catalysts

The catalysts work to convert the pollutants into unharmful compounds (Keith Hohn 2011). The VOCs and CO emissions present in the exhaust are converted to H_2O and CO_2 through an oxidation catalyst. A three-way catalyst removes oxygen from the NOx and converts it to N_2. While the three-way catalysts can reduce the NOx up to 90%, their effectiveness is insignificant for a lean-burn engine like the one being studied (T. J. Truex et al.). Another way to reduce NOx emissions to N_2 is by injecting ammonia or aqueous urea into the exhaust stream before the catalyst. This type of reduction is called selective catalytic reduction, and its installation and operation costs are too high (Hillier and Coombes 2004).

2.1.6 Natural Gas/Hydrogen Blends

Hydrogen can be added to natural gas fuel to address the issues of combustion performance and carbon-based emissions in natural gas-fired engines (Wang, Huang et al. 2007) (Thurnheer, Soltic et al. 2009, Zhang, Davis et al. 2022) (Akansu, Dulger et al. 2004). As CO, CO_2 and VOCs are produced due to carbon atoms in the carbon-based fuels, hydrogen fuels do not produce such emissions. However, using hydrogen alone as fuel is economically challenging as it requires modifications in the combustion chamber (Karim, Wierzba et al. 1996). Therefore, hydrogen is blended with natural gas to make use of its advantages in terms of better combustion performance and lower emissions. A drawback of Hythane (natural gas/hydrogen blended fuel) is that it generates higher in-cylinder temperatures and, as a result, higher NOx emissions. It can also cause damage to the combustion chamber material (Akansu, Dulger et al. 2004).

2.1.7 Pre-Combustion Chamber

Pre-Combustion Chamber (PCC) technology involves using a secondary combustion chamber installed on the cylinder head of the primary combustion chamber. A secondary supply of fuel-rich mixture is provided to the PCC for easier combustion. The combustion mixture in the PCC is used to ignite the leaner mixture in the primary combustion chamber. Even though the emissions are higher for richer combustion using PCC, the combustion performance and emissions decrease for leaner combustion (Yousefi, Gharehghani et al. 2015) (Keith Hohn 2011). A drawback of the PCC is the increased cost of cylinder head modification and the requirement of a secondary fuel system (Keith Hohn 2011).

2.1.8 High-Pressure Fuel Injection

High-pressure fuel injection technology is valid for Direct Injection engines. The fuel injected with higher pressure has greater momentum and mixes rapidly with the air inside the combustion chamber. This better mixing leads to better combustion performance and lowers CO and VOCs emissions (Minato, Tanaka et al. 2005). When combined with other emission reduction technologies, high-pressure fuel injection can reduce NOx levels up to 80%. However, the fuel injection system needs to be altered, and high-pressure fuel is also required (Keith Hohn 2011) (Chapman 2004).

2.2 The Integrated System

The emissions such as NOx, CO and VOCs for a SI engine highly depend on the AFR (Heywood 2018) (Baukal Jr 2012). For IC engines, a lambda sensor is installed on the exhaust manifold to measure the O_2 concentration and estimate the AFR of the burning mixture (Lauber, Guerra et al. 2011) (Grizzle, Dobbins et al. 1991) (Chang, Fekete et al. 1995). The NOx/O_2 sensor used in this research can

measure both NOx and O_2 simultaneously and for a wide range of O_2 concentrations in exhaust. Usually, the fuel injection is controlled to keep the AFR in the desired range (Alippi, de Russis et al. 2003) (Pace and Zhu 2010) (Anjum, Khan et al. 2017) (Li, Li et al. 2019). However, in two-stroke engines, the measurement and control of AFR is not a straightforward task because of scavenging and some air leaving the combustion chamber without participating in combustion. Because of this non-linearity in the behavior of engine w.r.t the AFR, a cost-effective integrated system is developed based on machine learning techniques for optimum engine emissions and combustion characteristics. The components of the integrated system include an air management package (AMP), an amperometric NOx/O_2 sensor, engine exhaust thermocouple, compressor suction and discharge pressure transducers, magnetic pickup sensor for speed (RPMs) and vibration sensors. The air management package includes an air bypass valve to divert the excess air from reaching the combustion zone. This system controls the bypass valve position rather than the fuel injection to achieve the desired AFR directly. The working of the engine and AMP is shown in Figure 2. Figures 3 and 4 show the components of the integrated system on the engine side of the whole unit.

2.3 Research Objectives

The current thesis presents an analysis of emissions and combustion characteristics for the effectiveness of the air management package implementation on an NGFRE. Moreover, a detailed study on the NOx/O_2 sensor including an electrochemical model and the utility of that model in terms of sensor degradation and calibration is also presented.

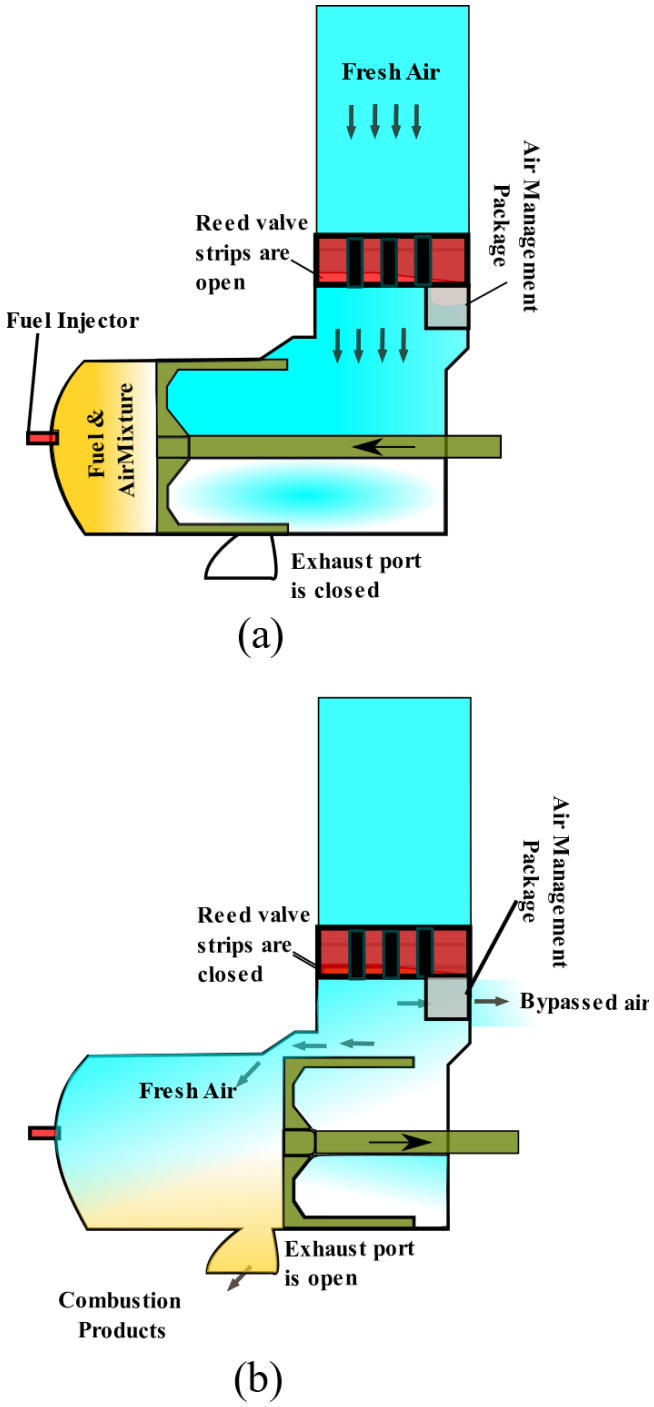

Figure 2. Schematic of Engine Operation. (a) Compression Stroke. (b) Expansion Stroke

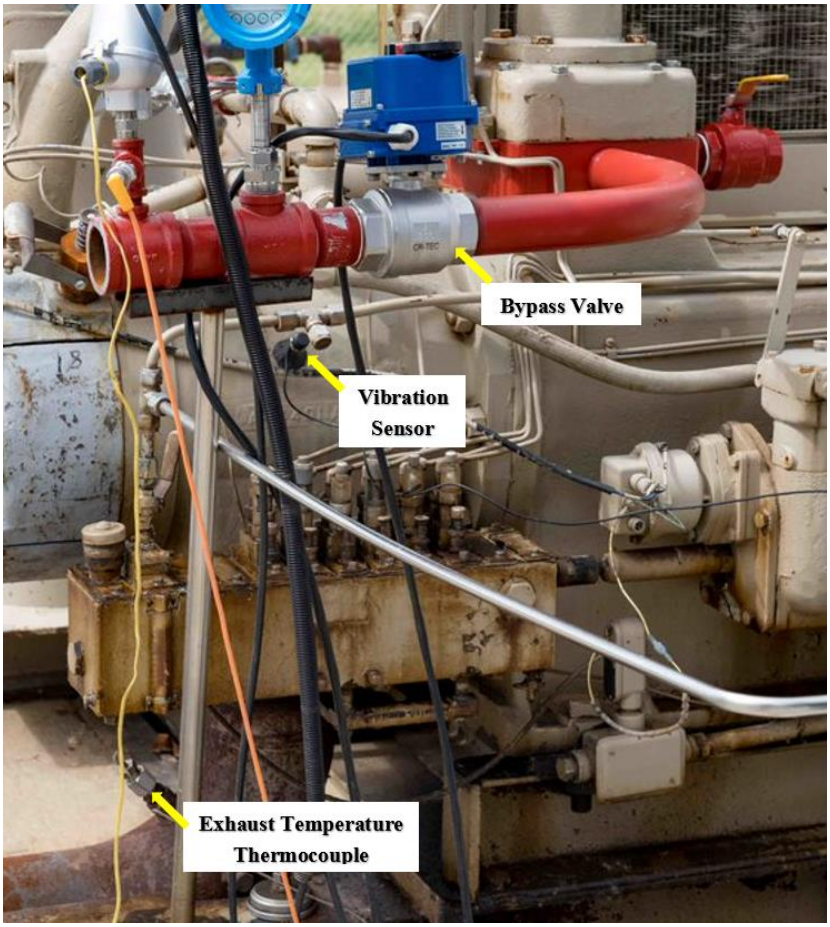

Figure 3. Components of the integrated system on engine side

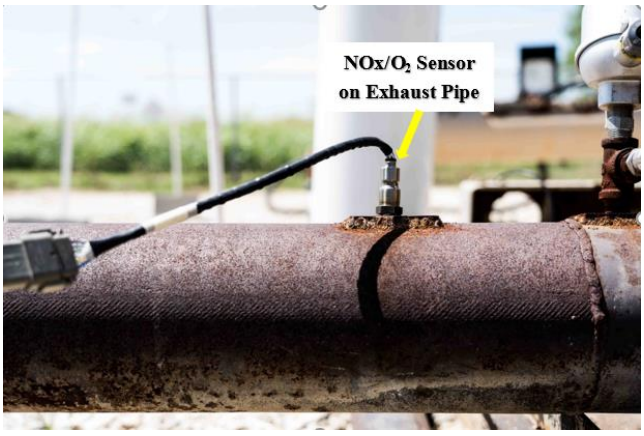

Figure 4. NOx/O_2 sensor

Chapter 3

Methods and Procedures

In this section, the experimental setup for the investigation of the integrated system is described. Each piece of equipment is explained as to what test parameter it measures and how it measures it. Real-life pictures are used to show the lab setup. Moreover, a detailed description of the data conversions and combustion analysis are also illustrated.

3.1 Experimental Setup

The experimental setup was located in the Natural Gas Lab of the University of Oklahoma. The engine was positioned in an open environment to replicate the real-life scenario of the field. The test engine specifications are detailed in Table 2. This engine is an integral compressor-engine unit i.e., a compressor is installed on the same crankshaft as the engine. The engine is run at different load steps and the effectiveness of the bypass mechanism is analyzed. The load is considered to be the brake horse power developed by the compressor as it is driven by the engine. Input parameters for specific engine load are estimated using PowerFlow sizing software by Cooper Machinery Services, which uses compressor suction and discharge pressures, RPMs and suction temperature to estimate the engine load. For this experiment, the natural gas is received from city supply lines.

The air bypass valve is an electronic proportional valve. The compressor parameters such as suction and discharge pressure and temperatures are measured by integrated k-type thermocouples and pressure transducers. Engine RPMs are recorded with a magnetic pickup sensor attached to the flywheel. The outputs of these sensors are fed to the programmable logic controller (PLC) by WAGO

Automation, USA and are displayed on e!COCKPIT HMI in real-time. Windrock 6400 portable engine analyzer is used to measure dynamic in-cylinder pressure data with respect to the crank angle. This analyzer relates the pressure data to the crank angle by utilizing the RPMs received from the encoder attached to the flywheel. It also provides immediate combustion variability parameters and spark plug data. A Coriolis mass flow meter is used to measure the fuel flow rate and another thermal mass flow meter is used for the propane mass flow rate.

Table 2. Engine Specifications

Engine Model	AJAX DPC-81
Engine Type	SI, Two-stroke, Naturally Aspirated, Water-cooled
Fuel	Natural Gas
Brake horsepower	81 bhp (61 kW)
Number of Cylinders	One
Bore	10.5 in 255 mm
Stroke	12 in 305 mm
Swept Volume	1039 in^3 17 liters
Combustion type	Lean-burn

An MKS 2030 Fourier Transform Infrared Spectroscopy (FTIR) device is used to measure the concentrations of species in the exhaust at two locations, i.e., before and after the catalyst. The FTIR is a highly accurate concentration detection method. Emission concentrations from this device can be viewed in real-time from the MG2000 software and can be stored in different formats. A drawback of this device is its inability to measure gases of higher concentrations i.e., O_2 and

N_2. Another portable device, Testo 300 flue gas analyzer, is used to measure O_2 concentration at a range of 0 to 21% at different locations in the exhaust.

When performing engine tests, the discharge pressure, suction pressure, and RPMs are set to the load desired as indicated by PowerFlow software. The engine operating conditions for each load are shown in Table 3. The emission data are recorded for different bypass valve positions during each load step. A time log is kept determining when the operating conditions are changed and when the engine is in a steady state after each variation in operating condition. Each measurement period is about 10-15 minutes, providing 40-60 data points for emissions and 120-180 data points for the engine operation parameters, which are averaged later. For each condition, the engine exhaust gas temperature from the thermocouple, ambient temperature, wind speed, and humidity are all recorded on a time log. Weather conditions are taken from the Mesonet application. All data analysis is conducted in Microsoft Excel. A schematic of the experimental setup is shown in Figure 5 and the lab setup, including the modifications to the engine intake, fuel line and bypass addition, and the individual measurement devices are shown in Figures 6 and 7.

Table 3. Experimental Conditions

Operating Parameters	Load		
	40%	60%	75%
Maximum Compressor Discharge Pressure (psi)	328	415	572
Average Compressor Suction Pressure (psi)	25	48	53
Engine Speed (RPMs)	375	441	445
Compressor Suction Temperature (^oF)	120	120	120

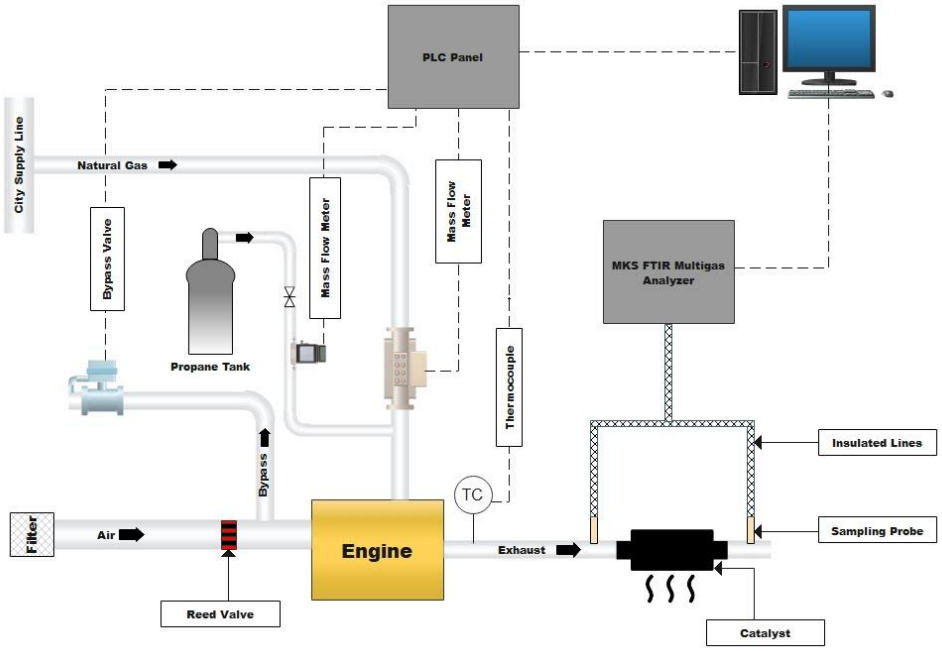

Figure 5. Schematic diagram of the test engine experimental setup

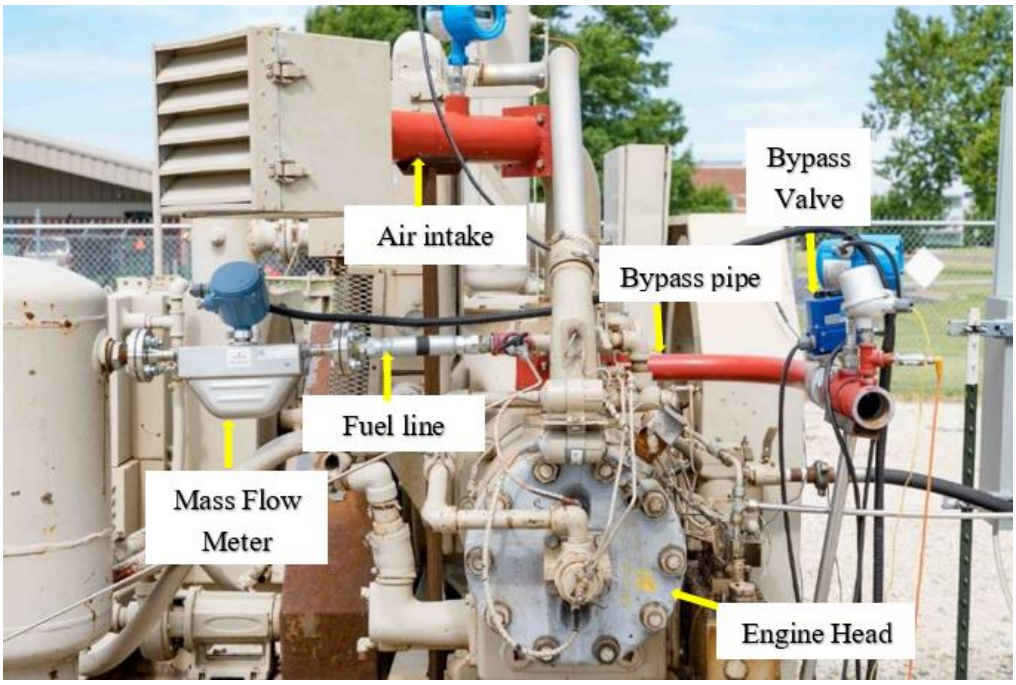

Figure 6. Modifications to engine air intake, fuel line and bypass addition

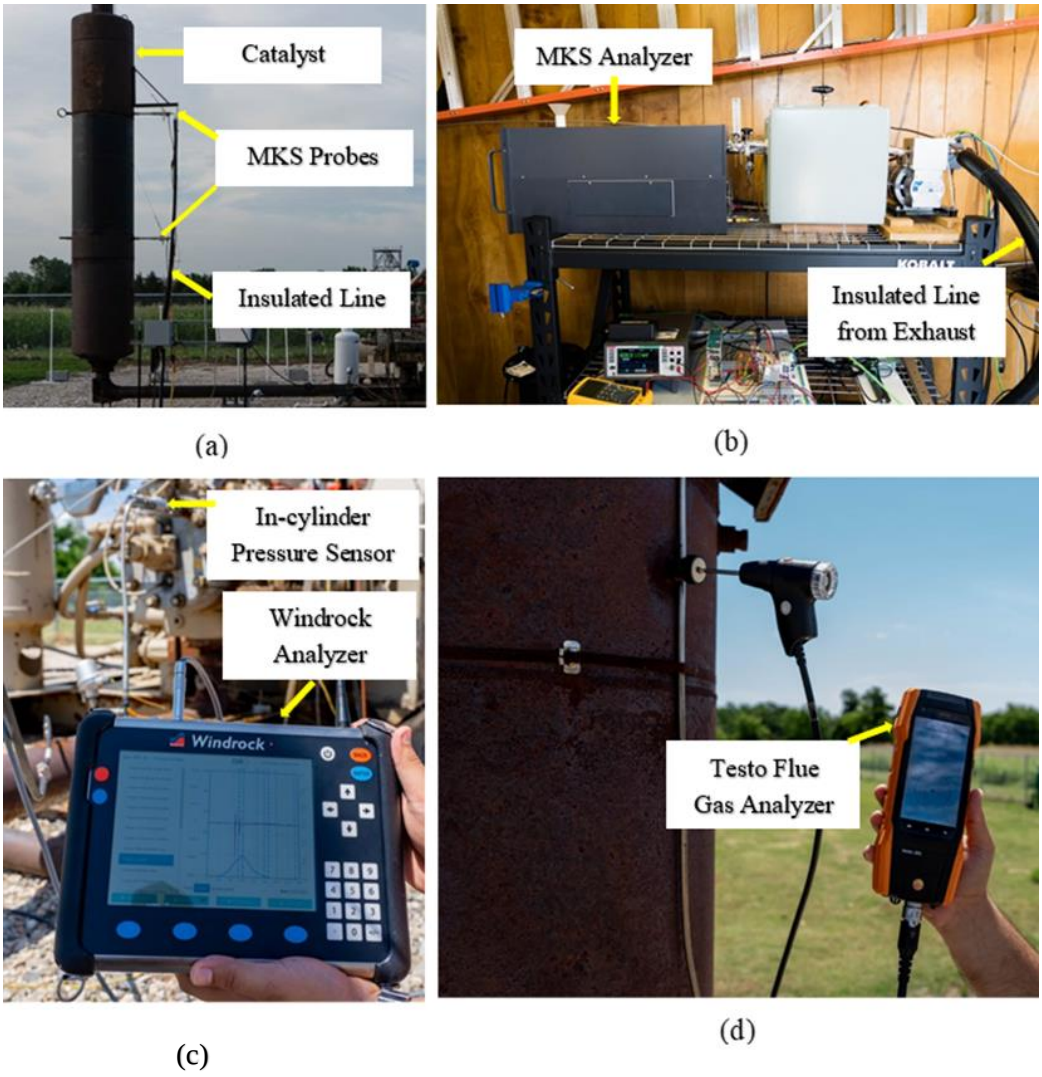

Figure 7. (a) MKS probes on the catalyst. (b) MKS Analyzer inside the Lab. (c) Windrock Portable Analyzer. (d) Testo Flue Gas Analyzer

3.1.1 External Bypass System

As shown in Figure 8, the external bypass system is installed on an external pipe that connects to the riser just beneath the reed valve, as explained previously. The butterfly valve used is a proportional valve, and its opening percentage can be controlled easily on a PLC.

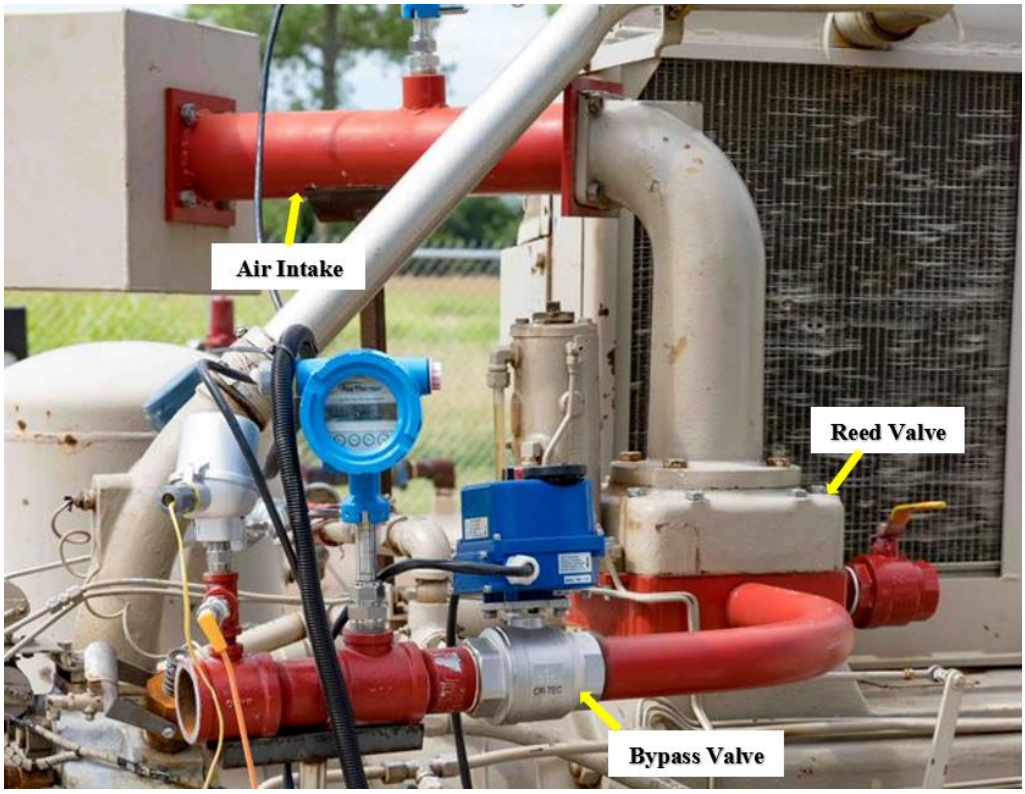

Figure 8. The external bypass valve assembly

3.1.2 External Bypass with Natural Gas/Propane Blends

As the current fuel supply is taken directly from the city supply line, it has less than 3% concentration of higher hydrocarbons. Therefore, the VOCs emissions produced are not as high as produced in the natural gas field locations. On the other hand, in the real-life scenario, the fuel is taken directly from other sources, such as the gas wells with much higher hydrocarbons concentrations than the clean city gas and result in higher VOCs emissions (i.e., over 100 ppm). To experimentally simulate the VOCs emissions from the field and analyze the effect of external bypass system, propane was blended with the natural gas fuel supply system and VOCs emissions were raised to more than 100 ppm. The experimental setup for propane addition is shown in Figure 9.

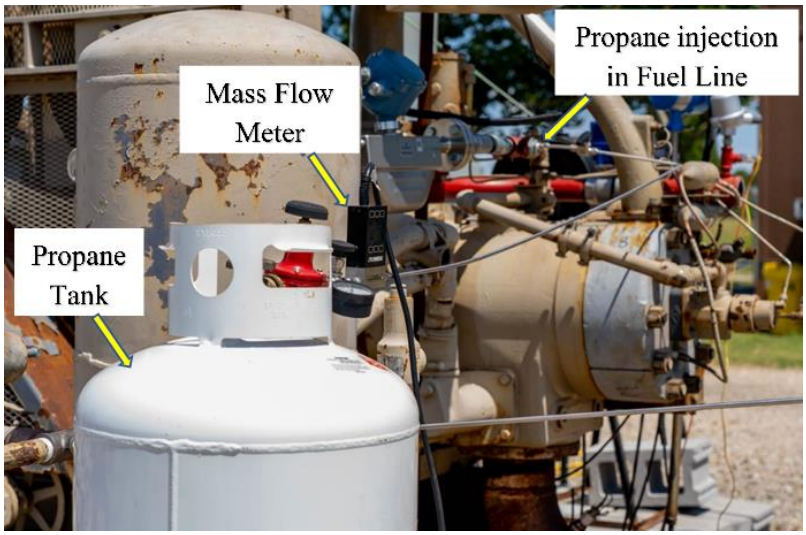

Figure 9. Propane injection setup

3.1.3 Internal Bypass System

Another test performed on the engine was the effect of internal bypass. The reed valve has six strips through which the air enters the cylinder. These strips are controlled by springs that open the valve during intake but close it during exhaust. If one of the strips is removed, some air escapes through the intake pipe and back into the atmosphere during the power stroke and does not make it to the combustion zone. The reed valve strips are shown in Figure 10.

Figure 10. Read valve strips

3.2 Combustion Metrics

The Standard deviation of peak pressure ($\sigma_{P_{peak}}$) was measured to evaluate the engine combustion stability in terms of cycle-to-cycle variability (CCV). The pressure values for each crank angle (CA) were collected for 250 cycles, and calculations were made. $\sigma_{P_{peak}}$ is a good measures of the CCV (Hoard and Rehagen 1997). These values are significant for part-load conditions as for a lean-burn engine; the CCV is very high under partial load. Also, the indicated mean effective pressure (IMEP) is calculated for 250 cycles and plotted. The IMEP plots provide a good visualization of the CCV. The IMEP is calculated using the following formula (Selamet, Rupal et al. 2004). Moreover, the coefficient of variation (COV) of IMEP is also calculated.

$$IMEP = \frac{\oint PdV}{V_{swept}} \qquad (4)$$

$$COV = \frac{\sigma_{IMEP}}{\overline{IMEP}} \qquad (5)$$

Where,

P = in-cylinder pressure at a particular CA

V_{swept} = swept volume of the cylinder

σ_{IMEP} = standard deviation of IMEP for 250 cycles

$\overline{IMEP}$ = average IMEP for 250 cycles

Moreover, the ITE is also calculated for the external bypass system for each 20% increment for bypass valve position and compared with the ITE of the original operation. The ITE of the engine is calculated using the following formula.

$$ITE = \frac{IMEP.V_{swept}.RPM}{60.\dot{m}_{fuel}.NCV} \qquad (6)$$

Where,

RPM = revolutions per minute

$\dot{m}_{fuel}$ = mass flow rate of fuel per second

NCV = net calorific value of fuel

Net Heat Release rate (HRR) curves are also calculated to analyze the behavior of NOx emissions. The HRR can be calculated using the following equation (Heywood 2018) (Gatowski, Balles et al. 1984).

$$\frac{d\dot{Q}}{d\theta} = \left(\frac{\gamma}{\gamma-1}\right) P \frac{dV}{d\theta} + \left(\frac{1}{\gamma-1}\right) V \frac{dP}{d\theta} + \dot{Q}_{cr} + \dot{Q}_{HT} \qquad (7)$$

Where

$\frac{d\dot{Q}}{d\theta}$ = gross heat release rate w.r.t the crank angle θ

γ = ratio of specific heats

$\dot{Q}_{cr}$ = heat lost to crevices

$\dot{Q}_{HT}$ = heat lost to cylinder walls

The value of γ is supposed to change during each cycle as it depends on the in-cylinder temperatures. The first two terms on the right-hand side of the equation represent the net HRR. It is the heat released that is transferred to the piston. The remaining terms represent the losses that occur in terms of combustion. For analysis of NOx emissions, the net HRR profile was plotted against the crank angle, assuming that the value of γ remains constant within the cylinder, and the relation to the NOx emissions was made.

3.3 Emissions Calculation

The exhaust emissions data were normalized to 15% O_2 and converted to dry-basis to compare with the EPA requirements (2021). Following formulas were used for the conversions.

$$x = x_{\text{exhaust}} \left(\frac{21-15}{21-O_{2,\text{exhaust}}} \right) \quad (8)$$

$$ppm = ppmvw \left(\frac{100}{100-\%age\ of\ H_2O_{exhaust}} \right) \quad (9)$$

Where,

x = normalized mole fraction of the gas in ppm

x_{exhaust} = mole fraction of the gas measured in ppm

$O_{2,\text{exhaust}}$ = mole fraction of O_2 in %

ppm = parts per million of the gas on dry basis

ppmvw = parts per million of the gas on wet basis

The precision uncertainties of the experimental data based on 95% confidence level are listed in Table 4 for each gas.

Table 4. Precision Uncertainties

	Gas				
	NOx	VOCs	CH_4	CO	CO_2
Uncertainties	±5.32 ppm	±0.162 ppm	±59.03 ppm	±0.11 ppm	±0.01 %

Chapter 4

Results and Discussion

In this section, the results obtained from the tests conducted on the AMP are discussed in detail. The engine was tested for three different cases i.e., with external bypass and internal bypass with only natural gas fuel, and external bypass with natural gas/propane blends as fuel. For each case, the engine was tested under 75%, 60% and 40% load steps. For 75% and 60% load steps, the external bypass valve could not be opened more than 60% and 40% respectively, due to the limitations in exhaust temperature.

4.1 Emissions Analysis for External Bypass System

The advantage of using an external bypass is that it does not hinder the incoming air so that the engine can run more efficiently. Moreover, it provides more options in terms of the amount of air bypassed as it is controlled externally as opposed to internal bypass where the dismantling of the intake system is required to access the reed valve. This feature provides better precession in terms of finding the optimum position of the bypass relative to the emissions. In current experiments, the bypass valve was opened with 20% increments until the allowable exhaust temperature limit i.e., 800^{o}F was reached, and the emissions and combustion data were collected.

4.1.1 NOx

The NOx emissions for each load step and for each bypass valve position are shown in Figure 11. A reduction of up to 23, 7 and 224 ppm was observed for NOx emissions at 75%, 60% and 40% loads respectively. It is clear from Figure 11 that

the minimum NOx emissions are produced at 100% bypass valve opening in case of 40% load. Even though the temperature at 100% bypass opened increases, the lower O_2 concentrations in the exhaust, as compared to bypass 0% opened, reduce the NOx emissions calculation significantly. The same could be said about the 75% load, but in the case of 60% load, the NOx emissions are optimum at 40% bypass valve opening. Moreover, for 40% load, the peak net heat release rate (HRR) is significantly higher at 40% bypass valve opening than that at 100% bypass opening, as shown in Figure 12. Here, 0°CA is the firing TDC. This higher HRR is also the reason behind the significant rise in NOx values at 40% and 60% bypass valve openings. At 60% and 75% loads, the net HRR curves do not vary much for different bypass valve openings and the NOx reduction for these loads corresponds to the O_2 concentration decrease in the exhaust.

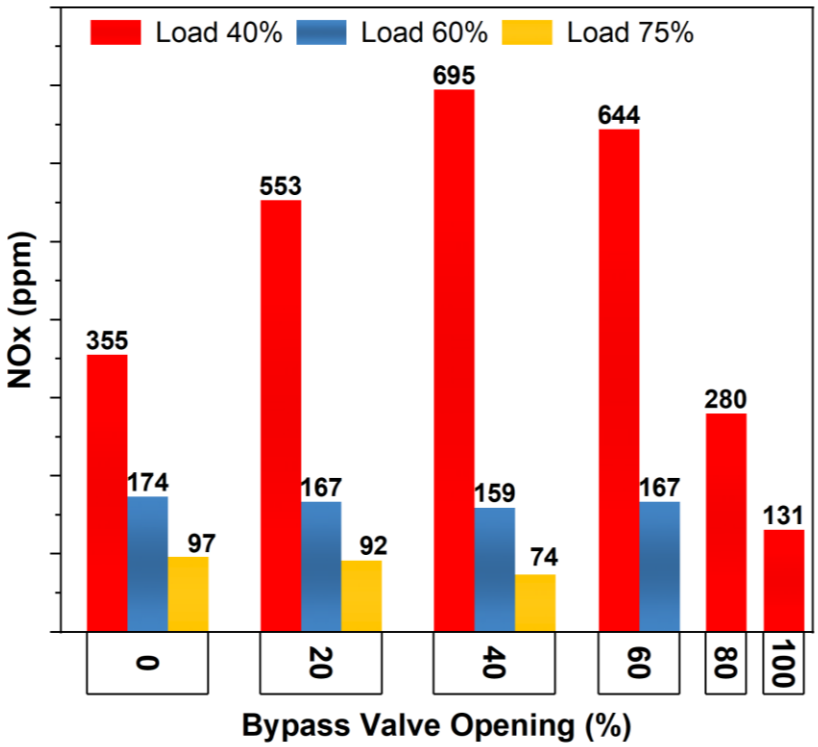

Figure 11. NOx emissions for different loads and bypass valve openings

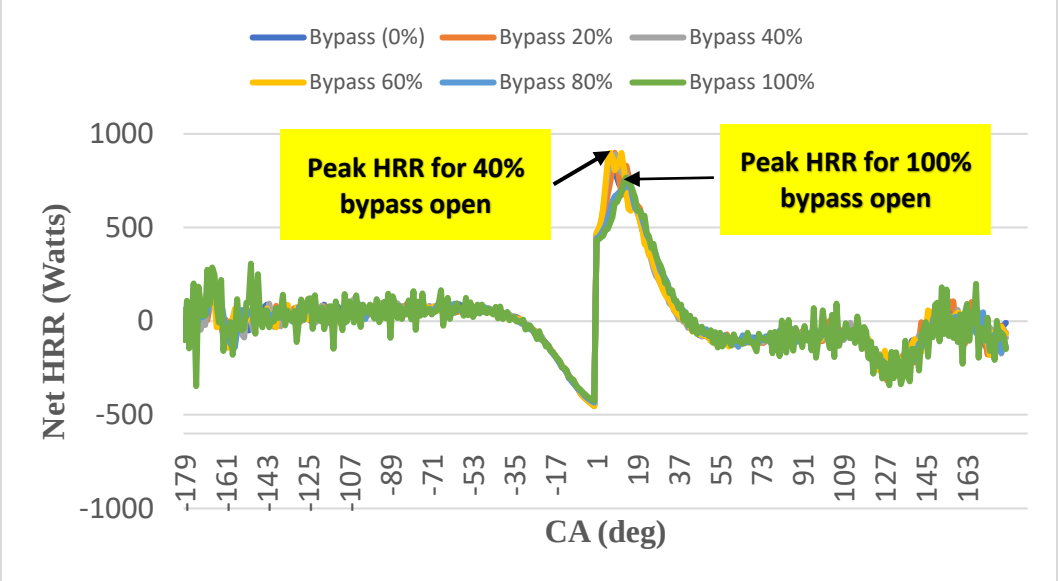

Figure 12. Net HRR curves at 40% load

4.1.2 VOCs

Figure 13 shows the variation in VOCs emissions with the bypass valve opening for different loads. A reduction of up to 28, 10 and 1 ppm was observed for VOCs emissions at 40%, 60% and 75% loads respectively. The VOCs emissions decrease with the bypass valve opening and are optimum at the maximum allowable bypass valve opening.

The most significant reduction can be seen in the case of 40% load because the catalyst efficiency also improves at higher exhaust temperatures. The effect of the bypass mechanism can be more significantly seen in the case of natural gas/propane blends as fuel, as the original VOCs produced during combustion are much higher. In this case, the reduction of VOCs is much more vital as compared to natural gas as fuel. This reduction in VOCs emissions substantiates the significance of the air management package.

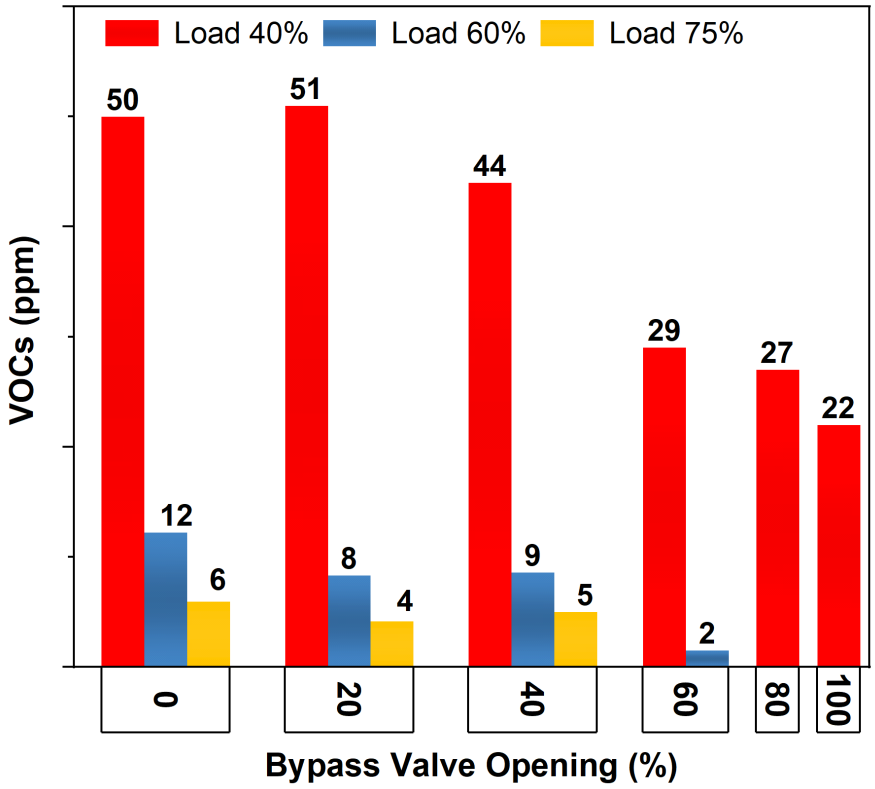

Figure 13. VOCs emissions for different loads and bypass valve openings

4.1.3 CO

Figure 14 shows the CO emissions vary abruptly for different loads with the bypass valve opening. At 40% load, the CO emissions increased significantly with the bypass valve opening and for 60% and 75% loads, they remained same and decreased up to 1 ppm, respectively. The increase in CO emissions at 40% load can be explained by the presence of insufficient oxygen (8.2% at 100% bypass valve opening) to convert CO to CO_2 in the catalyst. At higher loads, the CO emissions are oxidized in the catalyst as there is more oxygen (more than 12% at maximum allowable bypass valve opening) in the exhaust as compared to 40% load. The EPA

standards were not crossed even with the increased CO emissions at 40% load and higher bypass valve positions.

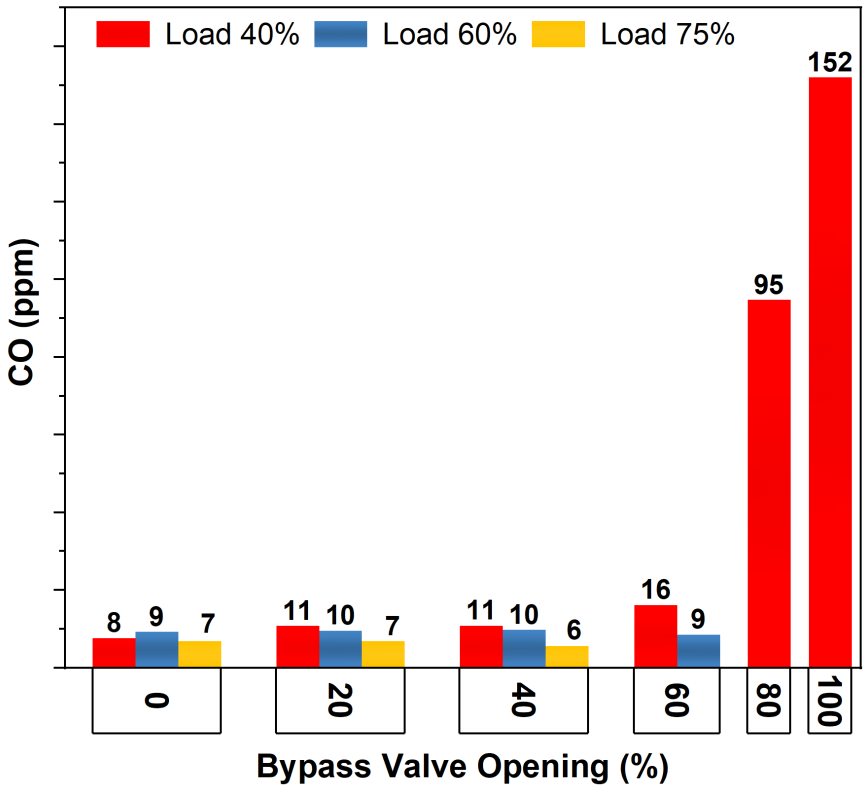

Figure 14. CO emissions for different loads and bypass valve openings

4.1.4 CH_4

Figure 15 shows a reduction of up to 8,955, 2,739 and 405 ppm for CH_4 emissions at 40%, 60% and 75% loads respectively. CH_4 reduction is by far the most significant achievement of the bypass mechanism. The optimum CH_4 emissions are produced at the highest allowable bypass valve opening. This reduction in CH_4 emissions is attributed to improved engine combustion performance at higher bypass valve openings. As the ITE and combustion stability improves with the

bypass valve opening, as shown in Figures 17 and 18, the amount of unburned fuel is reduced, resulting in lower CH_4 emissions.

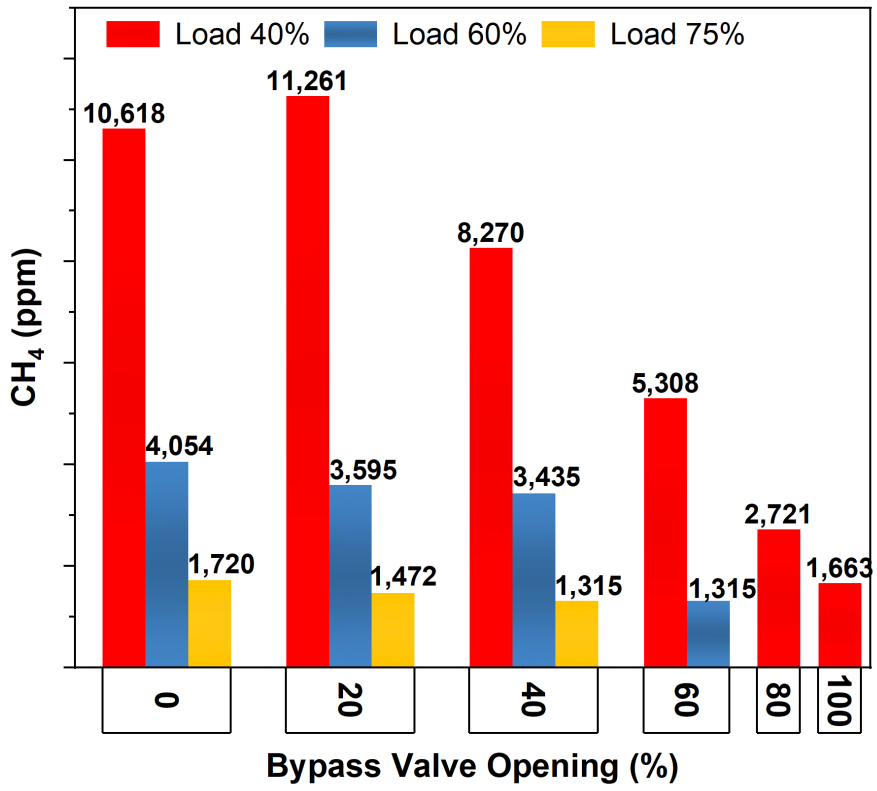

Figure 15. CH_4 emissions for different loads and bypass valve openings

4.1.5 CO_2

The CO_2 values increase for 40% and 75% loads up to 0.43 and 0.11%, whereas for 60% load they decrease by 0.2% as shown in Figure 16. The increase in CO_2 values is related to an increase in combustion performance/fuel utilization and the catalyst efficiency because both these processes produce CO_2. The highest increase in CO_2 values is for 40% load, which increases sharply after 60% bypass valve opening. This indicates better combustion performance, as seen in the ITE increase in Figure 17.

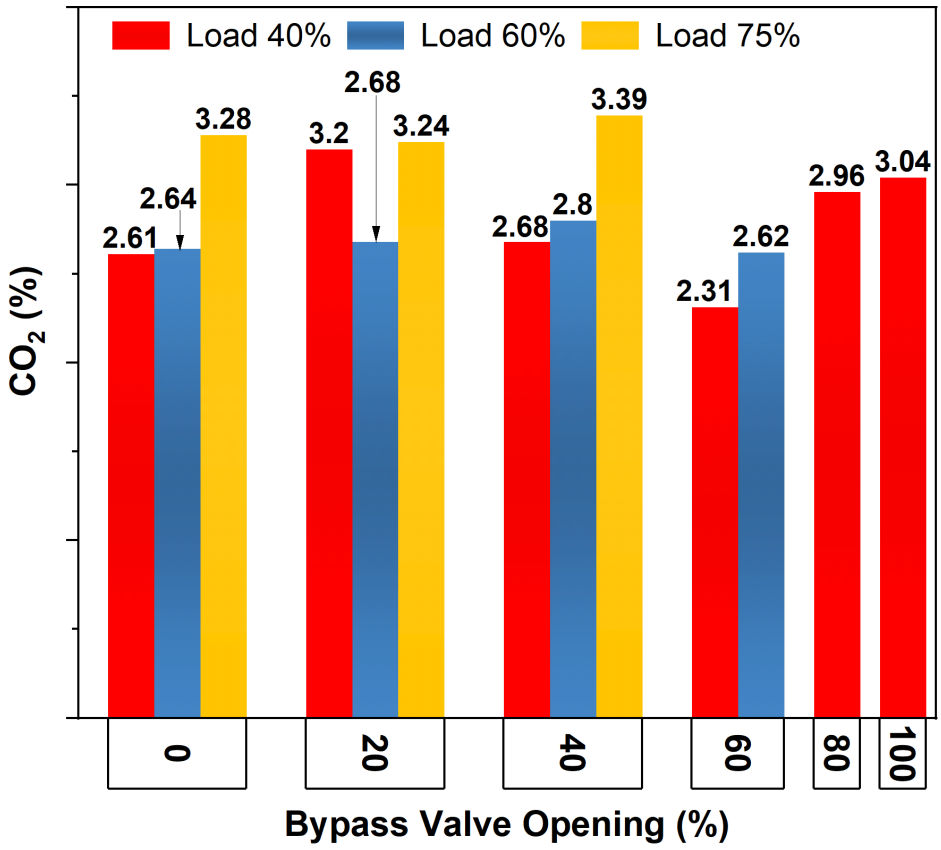

Figure 16. CO_2 emissions for different loads and bypass valve openings

4.2 Combustion Analysis for External Bypass System

Figures 17, 18 and 19 show that the combustion performance is optimum at the highest allowable limit for bypass valve opening. At 40% load, the ITE first drops and then improves significantly by 4.2% at 100% bypass valve opening, as shown in Figure 17. It is to be noted that the ITE is calculated based on the fuel supplied rather than the fuel trapped in the combustion zone. An increase in ITE indicates better utilization of the fuel supplied. In the case of higher loads, the ITE increases by 3.8% and 1.5% respectively for 60% and 75% loads, which is again a substantial improvement.

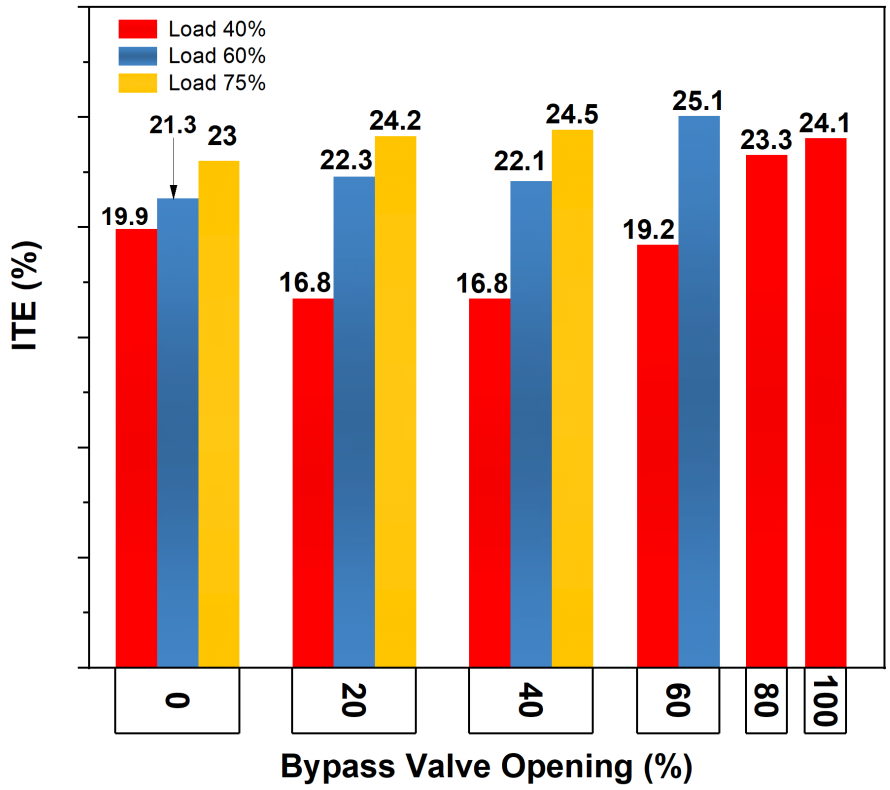

Figure 17. ITE for different loads and bypass valve openings

As shown in Figure 18, $\sigma_{P_{peak}}$ first increases with the bypass valve opening until 160 psi and then declines sharply to 63.6 psi for 40% load. Similarly, for 60% load, $\sigma_{P_{peak}}$ first increases from 61.5 psi to 76 psi at 20% bypass valve opening and then decreases to 49.4 psi at 60% bypass valve opening. For 75% load, the $\sigma_{P_{peak}}$ value declines consistently from 75.4 psi to 53.8 psi at 40% bypass valve opening. As the smaller value of $\sigma_{P_{peak}}$ indicates more stable combustion, this means that the combustion stability improves significantly with the bypass valve opening.

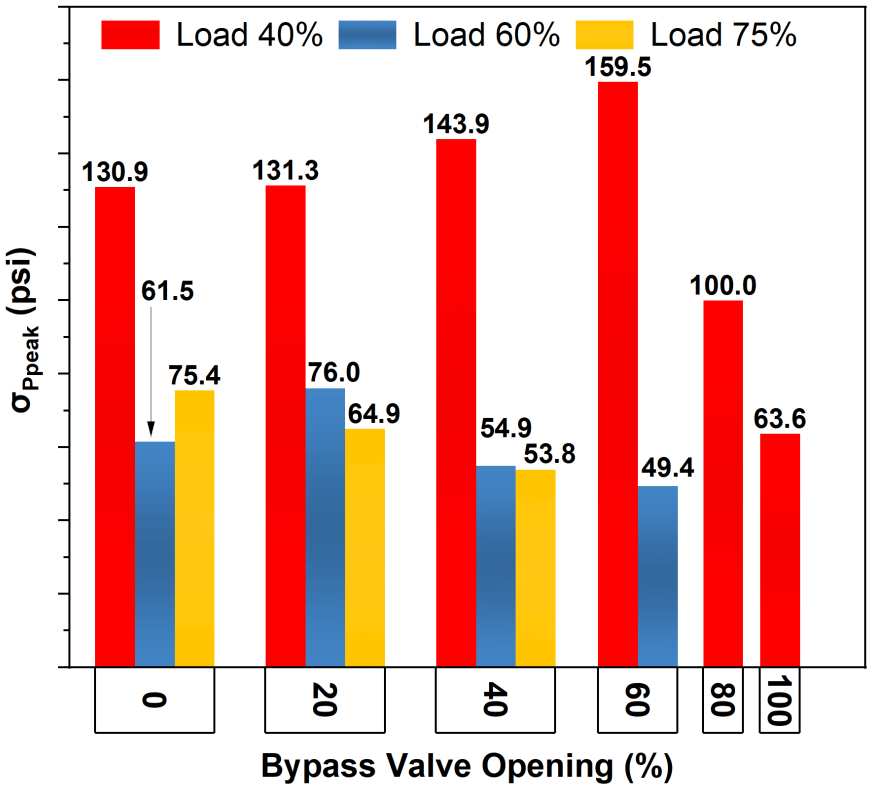

Figure 18. $\sigma_{P_{peak}}$ for different loads and bypass valve openings

In Figures 19, 20 and 21, the IMEP for each cycle has been plotted at each bypass valve location. As seen in these Figures, the combustion gets smoother and smoother with the bypass valve opening and is most stable at the maximum allowable bypass valve opening. Especially in the case of 40% load, the COV of IMEP reduces by 49%, which shows significant improvement in the combustion stability. Moreover, in the case of 60% and 75% loads, the COV of IMEP improves by 9% and 11% respectively, at the highest allowable bypass valve opening.

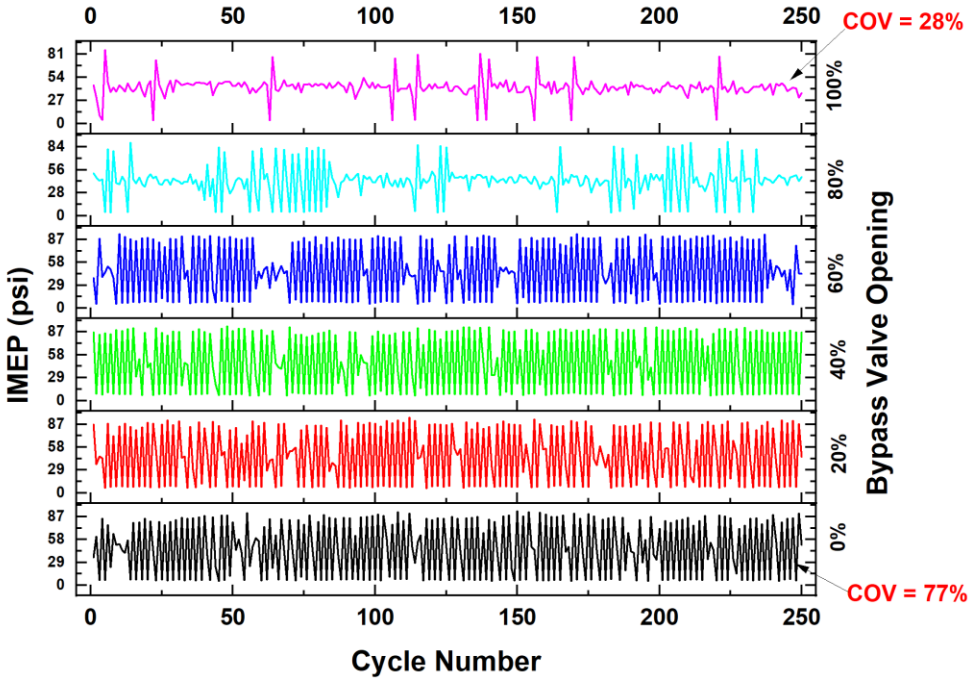

Figure 19. IMEP vs cycle number for each bypass valve position at 40% load

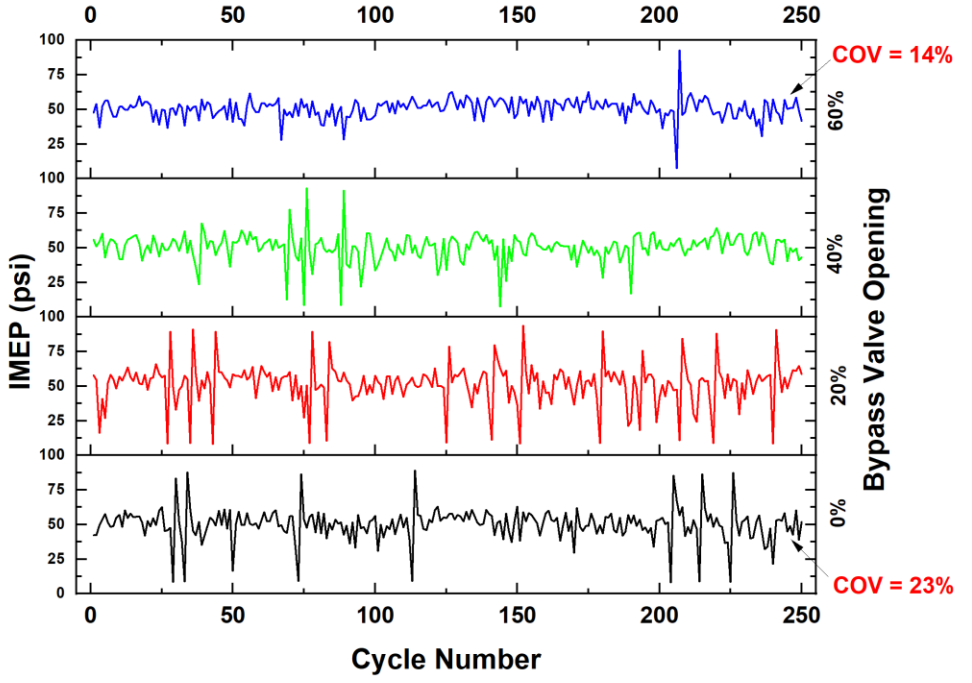

Figure 20. IMEP vs cycle number for each bypass valve position at 60% load

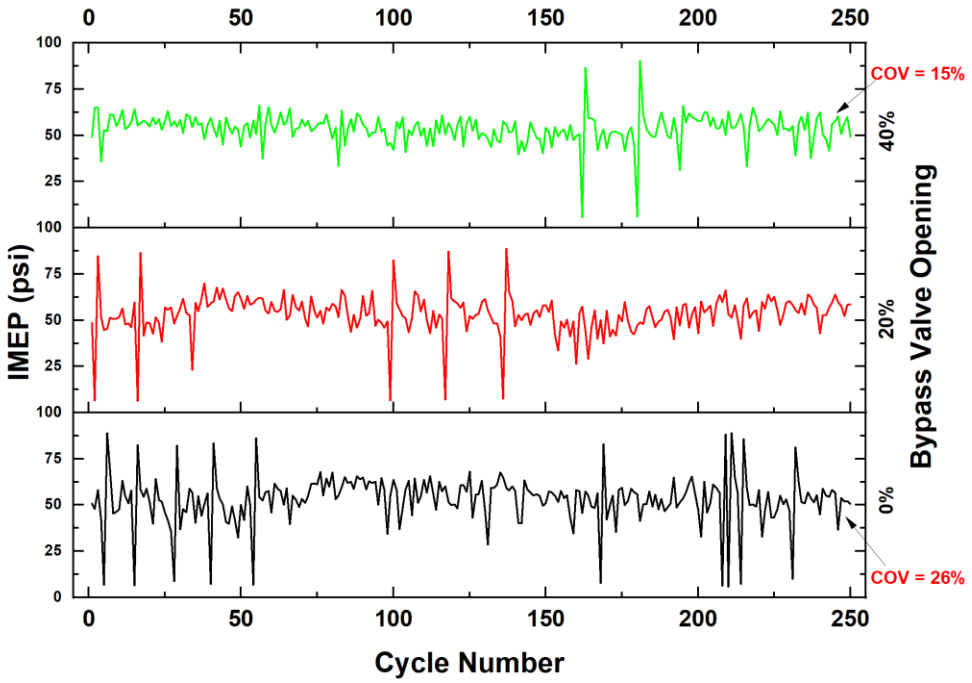

Figure 21. IMEP vs cycle number for each bypass valve position at 75% load

4.3 Internal Bypass System

The emissions data for the internal bypass mechanism are shown in Figure 22. A significant decrease in the CH_4, VOCs and NOx emissions occurred using the internal bypass. Whereas, for CO the emissions increased considerably while for CO_2, there was an increase in concentration at 40% load and a decrease at 60% load.

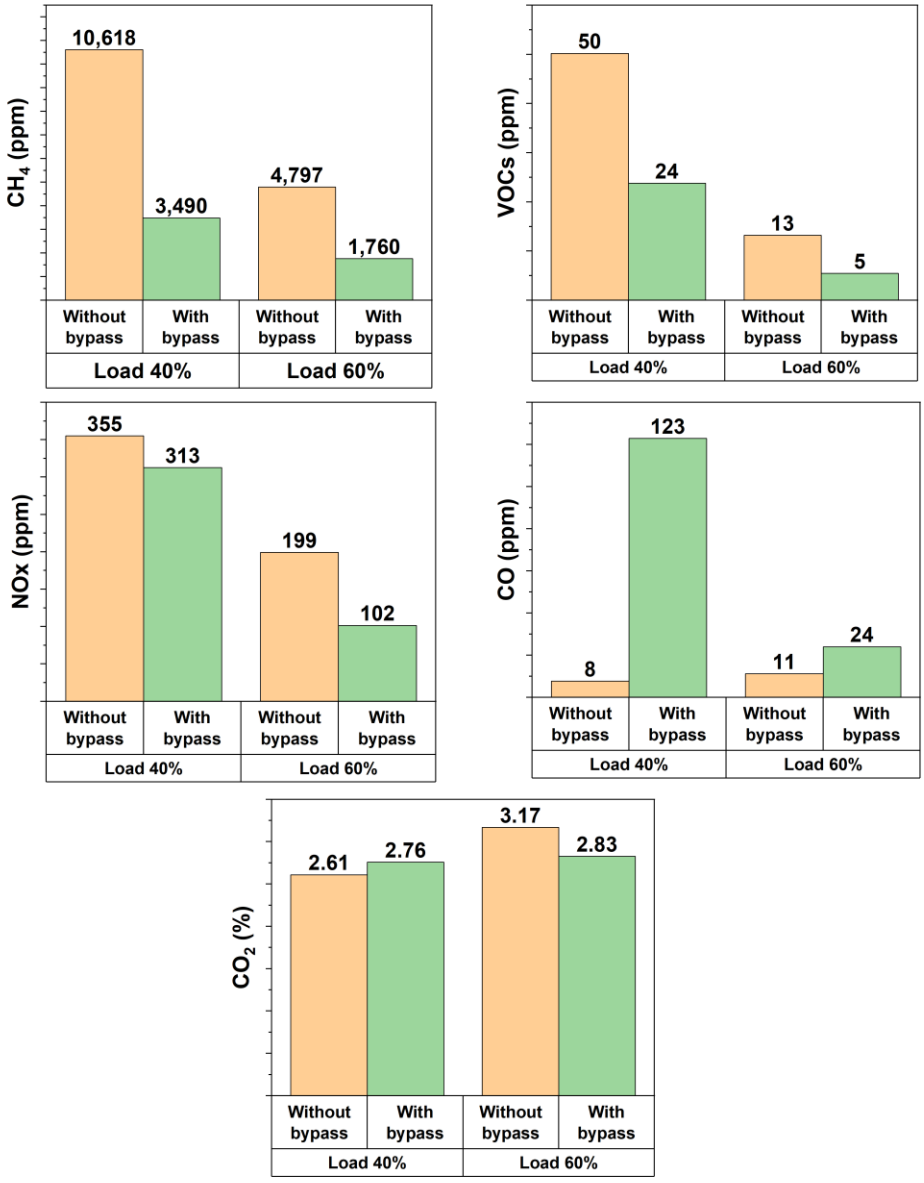

Figure 22. Emission data at 40% and 60% loads, with and without internal bypass

This test was performed for only one bypass condition i.e., 17% bypass, as only one strip was removed out of six (1/6% = 17%). Removing the second strip halts the engine as too much air escapes the combustion zone. Moreover, the incoming

air is hindered by the outgoing air and reduces the pressure difference required for intake. Another effect of removing the second strip is that the temperature limit (i.e., 800°F) for the exhaust pipe exceeds.

4.4 External Bypass with Natural Gas/Propane Blends

The results for the natural gas/propane blends are shown in Figures 23 and 24 for 40% and 60% loads respectively. The VOCs emissions are raised to more than 100 ppm for both the load steps, without the external bypass.

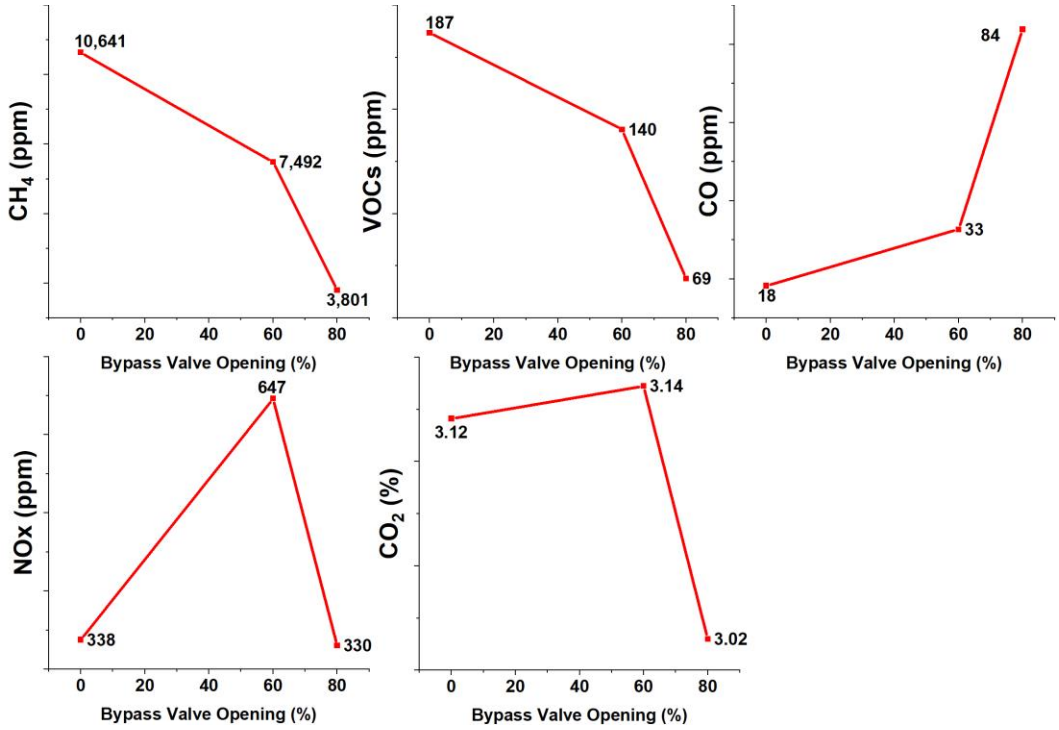

Figure 23. Emissions data for 40% load, with external bypass and natural gas/propane blends.

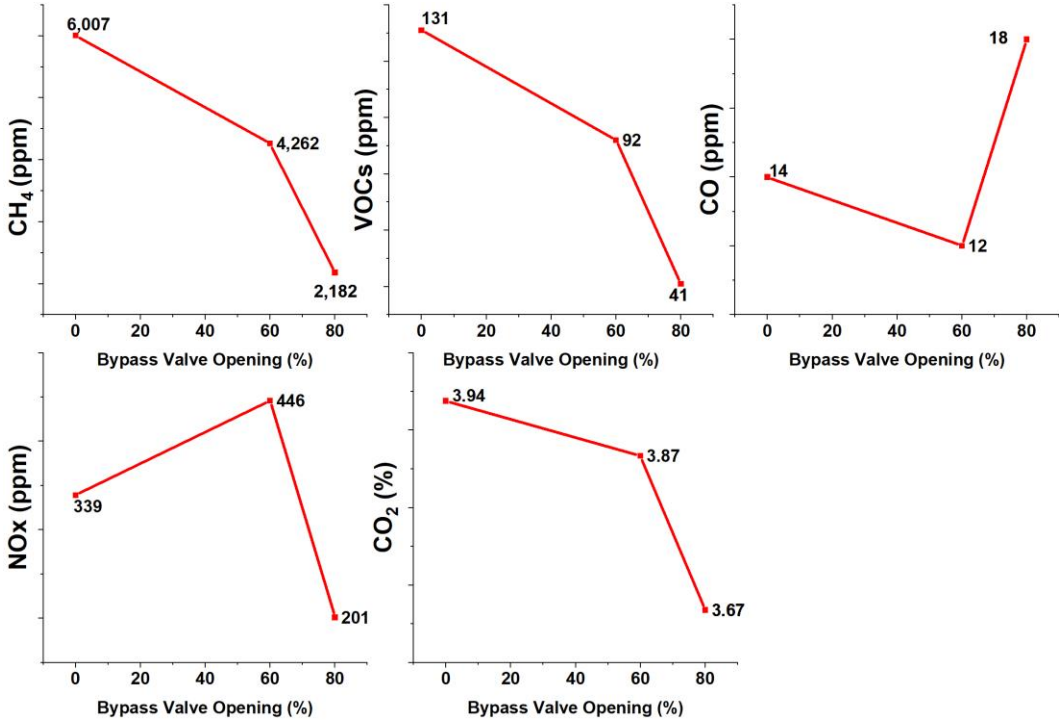

Figure 24. Emissions data for 60% load, with external bypass and natural gas/propane blends

By opening the bypass valve to 80%, the CH_4 and VOCs emissions reduce significantly to approximately 6,840 and 118 ppm respectively at 40% load. For NOx, the emissions do not reduce considerably, whereas, for CO, the emissions increase, indicating a decline in catalyst performance due to insufficient O_2. For 60% load, CH_4, VOCs and NOx emissions reduce significantly to 3,825, 90 and 138 ppm respectively, for a bypass valve opening of 80%. For CO, there is an increase in emissions as the bypass is opened to 80%.

At 80% bypass valve opening, the CO_2 drops for both 40% and 60% loads. This indicates that the incomplete conversion of higher hydrocarbons to CO_2 may be increasing the CO concentration in the exhaust gas.

Chapter 5

Amperometric sensor

5.1 Introduction

A solid-state gas sensor of amperometric type is used to measure O_2 and NOx concentrations in the exhaust. These sensors are widely used in automobiles to monitor the AFR of the combustion process through a closed-loop system and reduce unwanted emissions (Menil, Coillard et al. 2000) (Javed, Ramaiyan et al. 2018). An amperometric sensor operates in the limiting current region. The advantage of this is that the current is independent of voltage and is linearly proportional to the mole fraction of NOx and O_2 in the exhaust. This relation allows the measurement of a wide range of NOx and O_2 concentrations (Riegel, Neumann et al. 2002) (Aliramezani, Koch et al. 2019).

Solid-state sensors are based on electrochemical reactions in a solid electrolyte caused by concentration difference between two cavities/chambers connected to the electrolyte via electrodes (anode, cathode). These reactions involve the flow of electronic current between these electrodes and generate a voltage. Earlier narrow-band or potentiometric sensors were based on this principle i.e. measurement of voltage (Vs) generated by concentration difference of oxygen in the exhaust stream and in ambient air (Moos 2005). The disadvantage of this type of sensor was that it could only determine the stoichiometric AFR as the voltage changes only at this point. Away from the stoichiometric AFR, the voltage remains the same. The output signal of a typical potentiometric sensor is shown in Figure 25 (Menil, Coillard et al. 2000) (Engh and Wallman 1977) (Docquier and Candel 2002).

To compensate for this, a wide-band or amperometric sensor was introduced. Due to a very high diffusion coefficient of O_2 in gases, a diffusion barrier is added to the exhaust stream's path to control the amount of O_2 inside the measuring chamber. A pumping voltage is applied to pump oxygen out of the exhaust stream that passes the diffusion barrier. This voltage operates in the limiting current region. The limiting current generated because of this pumping voltage is proportional to the concentration of oxygen in the exhaust stream. An output signal of a typical amperometric sensor is shown in Figure 26 (Moos 2005) (Menil, Coillard et al. 2000).

A similar approach is used to measure NOx emissions in the exhaust stream. On one electrode NOx emissions are reduced to N_2 and O_2 and the resulting oxygen ions convert to oxygen molecules in the reference chamber filled with ambient air.

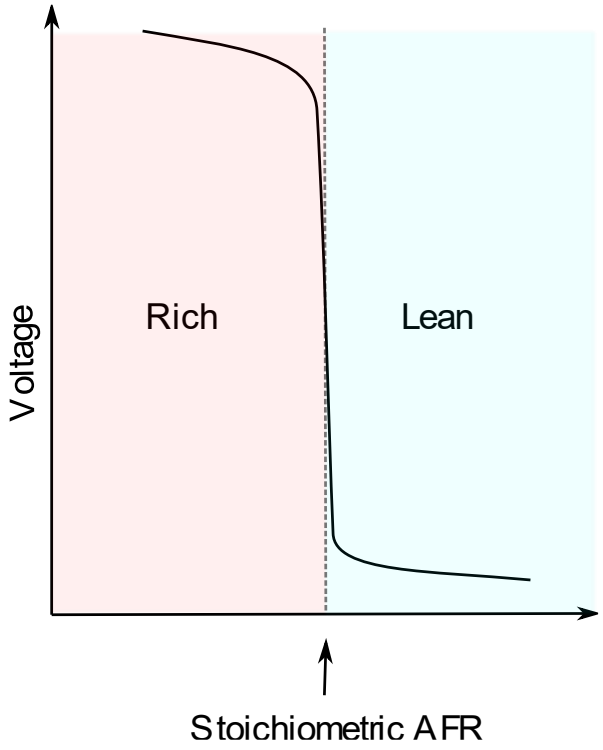

Figure 25. A typical response of a potentiometric sensor

So, measuring O_2 essentially gives a prediction of the NOx concentration. However, O_2 must be removed from the exhaust stream for this mechanism to work. By doing so, both O_2 and NOx can be measured simultaneously.

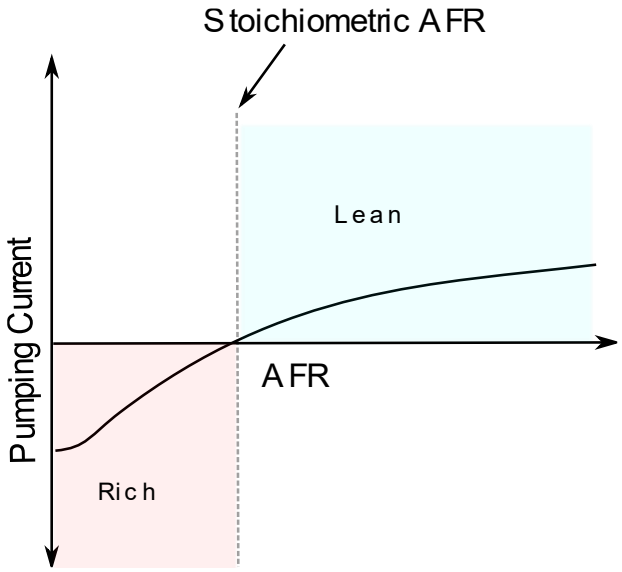

Figure 26. A typical response of an amperometric sensor

The sensor discussed in this thesis is an amperometric NOx/O_2 sensor that measures both O_2 and NOx simultaneously. It comprises three chambers and two diffusion barriers. The exhaust stream flows through the first diffusion barrier into the first chamber, where O_2 is pumped out by applying a voltage V_{P1}. Another reaction occurring in this chamber is the reduction of NO_2 to NO. Therefore, all the NOx after the first chamber would have been converted to NO only. The remaining species flow through the second diffusion barrier and into the second chamber, where NO is reduced by applying voltage V_{P2} and the resulting O_2 goes into the reference chamber. A fixed voltage Vs is maintained between first and reference chambers which corresponds to the stoichiometric voltage as in the potentiometric sensor. A schematic diagram of an amperometric NOx/O_2 senor is shown in Figure 27.

In this section of the thesis, an electrochemical model for an amperometric NOx/O_2 sensor is developed and the current-voltage (I-V) curves generated through the electrochemical model and their significance in understanding the deterioration of the electrode material of the sensor are discussed in detail. Moreover, for low mole fractions of NOx (<100 ppm), the amount of current produced is in the range of nanoamperes to microamperes and can be highly affected by the presence of excess O_2 and other gases (Riegel, Neumann et al. 2002). Therefore, a calibration method for the amperometric sensor utilized by (Aliramezani, Koch et al. 2019) and (Li and Tang 2012) is presented in the presence of high mole fractions of excess O_2 (14% - 15%).

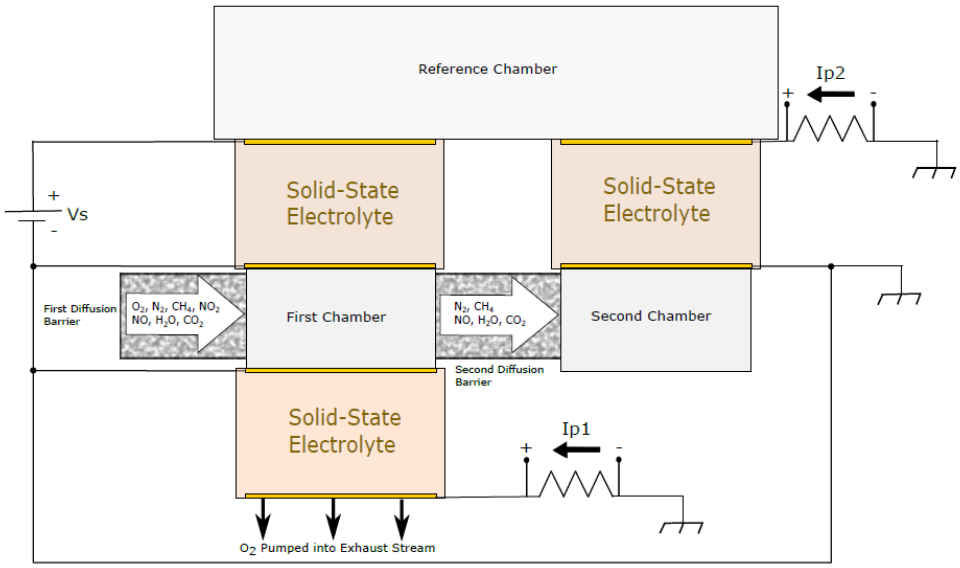

Figure 27. Schematic of an amperometric NOx/O_2 sensor

5.2 Electrode Polarization/Overpotential in an Amperometric Sensor

It is crucial to understand the reaction kinetics resulting from pumping voltage to predict the output of an amperometric sensor. A basic understanding of Solid Oxide

Fuel Cells (SOFCs) is pivotal in internalizing the concept of electrode kinetics of an amperometric sensor. At first, there is no reduction as the pumping voltage is less than the activation energy required for reduction. After the activation barrier is crossed, the current begins to flow. As the activation polarization region ends, the cell resistance becomes dominant and the current is almost linear to the voltage. After a certain voltage, the concentration of the desired species gets very low at the cathode and the current stops increasing linearly with the voltage. At this point, the current is independent of the voltage and only depends on the concentration of the desired species. This region is called the limiting current region, which is significant as the current is linearly dependent on the concentration of the species under observation. Increasing the voltage beyond the limiting current region may cause damage to the electrode material and is dangerous to the sensor (Aliramezani, Koch et al. 2019). A typical I-V characteristic curve of an amperometric sensor is shown in Figure 28 (Menil, Coillard et al. 2000) (Riegel, Neumann et al. 2002) (Aliramezani, Koch et al. 2019) (Docquier and Candel 2002) (Benammar 1994) (Betteridge 2006) (Pham and Glass 1997) (Dietz 1982) (Coillard, Juste et al. 2000) (Ono, Shimanoe et al. 2000).

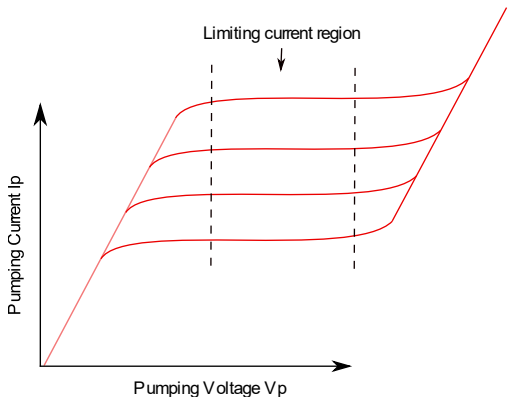

Figure 28. Characteristic I-V curves for an amperometric sensor

5.3 Methodology

The model is based on electrochemical and diffusion mechanisms. Nernst equations are used to express pumping voltages in each cell. Butler-Volmer equation (B-V) and Tafel equation are used to describe activation overpotential. Faraday's law and Fick's law are utilized for the explanation of the diffusion/mass transport mechanism. Additionally, concentration losses have been added to Nernst equations in terms of limiting current in each cell.

5.3.1 Nernst Voltages

The Nernst equation is a well-established tool that is supported by a massive number of experimental validations (Feiner and McEvoy 1994). It is used to determine the chemical potential of a redox (oxidation-reduction) reaction. The generic form of the Nernst equation is given below (Fernández-Solis, Vimalanandan et al. 2016) (Lefrou, Fabry et al. 2012) (del Olmo, Pavelka et al. 2021).

$$V = E^0 - \frac{\mathrm{RT}}{\mathrm{nF}} \ln\left(\frac{\prod_{prod} \mathrm{x}_{prod}^{v_i}}{\prod_{react} \mathrm{x}_{react}^{v_j}}\right) \qquad (10)$$

Where,

E^0 = cell potential when the concentration of all ions is 1 moles per liter

F = Faraday’s constant

T = temperature of exhaust gases

R = universal gas constant

n = number of electrons involved in the reaction

v_i, v_j = stoichiometric coefficients of species *i* and *j* respectively

$x =$ mole fraction by volume of each species

E^0 can be represented in terms of E_0^0 which is the E^0 that would have been developed if the reactions were taking place at standard conditions (298K, 1atm) (Amphlett, Baumert et al. 1995) (Sharma, Ahmed et al. 2018).

$$E^0 = E_0^0 + (T - T_0)\frac{\Delta S}{nF} \qquad (11)$$

Where,

T_0 = standard temperature (298K)

ΔS = entropy change of reaction

Equation (1) presents an ideal voltage which is termed as open circuit voltage. But in reality, there are some losses affiliated with the electrochemical process such as activation, ohmic and concentration losses which need to be excluded from ideal voltage (Aliramezani, Koch et al. 2019) (Mann, Amphlett et al. 2000) (Haji 2011) (Etsell and Flengas 1971) (Noren and Hoffman 2005) (Zhao and Virkar 2005).

$$V = E_0^0 + (T - T_0)\frac{\Delta S}{nF} - \frac{R\mathrm{T}}{\mathrm{nF}}\ln\left(\frac{\prod_{prod} \mathrm{x}_{prod}^{v_i}}{\prod_{react} \mathrm{x}_{react}^{v_j}}\right) - \eta_\mathrm{a} - \eta_\mathrm{o} - \eta_\mathrm{c} \qquad (12)$$

Where,

$\eta_\mathrm{a} =$ activation losses

$\eta_\mathrm{o} =$ ohmic losses

$\eta_\mathrm{c} =$ concentration losses

The term "loss" is also referred to as "overpotential" or "polarization" whenever dealing with electrochemical reactions.

5.3.2 Oxygen Pumping Cell

In the case of lean combustion, the exhaust gases, including oxygen, flow through the diffusion barrier into the first chamber. The concentration of oxygen in the reference chamber is known (usually ambient air). The voltage V_S is kept at a constant value which refers to the stoichiometric condition. To keep this voltage constant, a pumping current is used to either pump oxygen into or out of the first chamber so that the concentration gradient between the two chambers remains the same. This pumping current is the output of the oxygen measuring cell and is proportional to the amount of oxygen diffused into the first chamber.

In the case of stoichiometric combustion, there is no oxygen flowing in the first chamber and the voltage remains unchanged and no current flows in the cell.

In the case of rich combustion, the oxygen molecules try to move from higher pressure i.e., the first chamber, through the diffusion barrier and into the exhaust stream. To keep the concentration gradient constant between the first and reference chambers, the pumping current now flows in the opposite direction and water molecules from the exhaust stream are decomposed to bring oxygen into first chamber (Collings, Hegarty et al. 2012).

Vs can be estimated using Nernst equation (Moos 2005) (Moseley 1997) (Riegel, Neumann et al. 2002) (Collings, Hegarty et al. 2012) (Aliramezani, Koch et al. 2017). This is the same voltage signal that is generated in a potentiometric sensor.

$$V_S = -\frac{\mathrm{RT}}{2\mathrm{F}} \ln\left(\frac{x_{O_2,fc}^{0.5}}{x_{O_2,rc}^{0.5}}\right) \qquad (13)$$

Where,

$x_{O_2,rc}$ = mole fraction of O_2 in the reference chamber

$x_{O_2,fc}$ = mole fraction of O_2 in the first chamber

As the NGFRE being studied is a lean-burn engine, the oxygen pumping cell is modeled for lean AFR. Following reactions occur in the O_2 pumping cell:

- $\frac{1}{2}O_{2(x_{O2,fc})} + 2e^- \rightarrow O^{2-}$ (Reduction)
- $O^{2-} \rightarrow \frac{1}{2}O_{2(x_{O2,env})} + 2e^-$ (Oxidation)
- $\frac{1}{2}O_{2(x_{O2,fc})} \rightarrow \frac{1}{2}O_{2(x_{O2,env})}$ (Overall)

The electrochemical reaction can be expressed by the Nernst equation as follows.

$$V_{P1} = -\left[\mathrm{E_{fc}^o} + \frac{\Delta \mathrm{S_{ox-red,fc}}}{2\mathrm{F}}(\mathrm{T} - \mathrm{T_o}) - \frac{\mathrm{RT}}{2\mathrm{F}}\ln\left(\frac{x_{O_2,env}^{0.5}}{x_{O_2,fc}^{0.5}}\right) - \eta_{\mathrm{a1}} - \eta_{\mathrm{o1}} - \eta_{\mathrm{c1}}\right] \quad (14)$$

Where,

$\mathrm{E_{fc}^o}$ = open circuit potential at standard state (298K, 1atm) for the first chamber

$\Delta \mathrm{S_{ox-red,fc}}$ = entropy change of reaction for the first chamber

$x_{O_2,env}$ = mole fraction of O_2 in the exhaust stream

The subscript 1 represents the first chamber. The negative sign indicates that the voltage V_{P1} is an input as opposed to Vs, which is an output. The value of $\mathrm{E_{fc}^o}$ can be calculated by forming a galvanic cell with a standard hydrogen electrode (SHE). The SHE potential is 0V by convention, so the voltage developed in this galvanic cell is the open circuit potential of the electrode at the standard state. The value of $\Delta \mathrm{S_{ox-red,fc}}$ can be estimated by the following equation (Aliramezani, Koch et al. 2019).

$$\Delta \mathrm{S_{ox-red}} \approx \Delta S_{ox-red}^0 = \sum_{prod} v_i \Delta S_i^0 - \sum_{react} v_j \Delta S_j^0 \quad (15)$$

Where,

ΔS^{0}_{ox-red} = entropy change of reaction at standard state

The important thing is that the current generated by the conversion of NO_2 to NO in the first chamber has a negligible effect on V_{P1} and I_{P1} as the mole fraction of NO_2 is in parts per million which is very low as compared to O_2, which is in percentage.

5.3.3 NOx measuring Cell

NOx emissions are measured in the second chamber where the exhaust species, excluding O_2, enter through the second diffusion barrier after all the NO_2 is reduced to NO in the first cell. Here NO is reduced to O_2 at the cathode, which then moves through the electrolyte to the anode, where it enters the reference chamber. The current I_{P2} which is generated in this process is the output and is proportional to the amount of NOx in the exhaust stream.

Following reactions take place in the NOx measuring cell.

- $O^{2-} \rightarrow \frac{1}{2} O_{2(x_{O2,rc})} + 2e^{-}$ (Oxidation)
- $NO + 2e^{-} \rightarrow \frac{1}{2} N_2 + O^{2-}$ (Reduction)
- $NO \rightarrow \frac{1}{2} N_2 + \frac{1}{2} O_{2(x_{O2,rc})}$ (Overall)

The Nernst equation for NOx measuring cell is given below.

$$V_{P2} = -\left[\mathrm{E^{o}_{sc}} + \frac{\Delta \mathrm{S_{ox-red,sc}}}{2\mathrm{F}}(\mathrm{T} - \mathrm{T_o}) - \frac{R\mathrm{T}}{2\mathrm{F}} \ln\left(\frac{\mathrm{x^{0.5}_{O_2,rc}} \cdot \mathrm{x^{0.5}_{N_2,rc}}}{\mathrm{x_{NO,sc}}}\right) - \eta_{a2} - \eta_{O2} - \eta_{c2}\right] \quad (16)$$

Where,

$\mathrm{E^{o}_{sc}}$ = open circuit potential at standard state (298K, 1atm) for the second chamber

$\Delta S_{ox-red,sc}$ = entropy change of reaction for the second chamber

$x_{N_2,rc}$ = mole fraction of N_2 in the reference chamber

$x_{NO,sc}$ = mole fraction of NO in the second chamber

The subscript 2 means the second chamber.

5.3.4 Activation Losses

Activation losses are associated with the minimum voltage required for the redox reactions to begin. This voltage is required to overcome the energy barrier at the electrode/electrolyte interface. The general B-V equation is the governing equation used to calculate activation losses (Aliramezani, Koch et al. 2019) (Noren and Hoffman 2005) (Yonekura, Tachikawa et al. 2011). At higher voltages (V>200mV), the Tafel approximation can be used to avoid computational cost because of B-V equation's complexity (Aliramezani, Koch et al. 2019) (Fernández-Solis, Vimalanandan et al. 2016) (Noren and Hoffman 2005).

5.3.5 First Chamber

For the first cell, VP1 is assumed to be high enough to use the Tafel equation given below (Aliramezani, Koch et al. 2019).

$$\eta_{a1} = \frac{RT}{\alpha_1 F} \ln\left(\frac{i_{P1}}{i_{P1}^0}\right) \qquad (17)$$

Where,

α_1 = first chamber charge transfer coefficient

i_{P1}^0 = reference exchange current density for the first chamber

i_{P1} = first chamber pumping current density

5.3.6 Second Chamber

For the second chamber, B-V equation is utilized as given below (Aliramezani, Koch et al. 2019) (Aliramezani and Koch 2021).

$$i_{p2} = i_{p2}^{o}\left(\frac{x_{NO,sc}}{x_{NO,sc}^{o}}\right)^{\gamma}\left[\exp\left(\frac{\alpha_{a2}F}{\bar{R}T}\eta_{a2}\right) - \exp\left(\frac{-\alpha_{c2}F}{\bar{R}T}\eta_{a2}\right)\right] \quad (18)$$

Where,

i_{p2} = second chamber pumping current density

i_{p2}^{o} = reference exchange current density for second chamber

$x_{NO,sc}$ = NO mole fraction in second chamber

$x_{NO,sc}^{o}$ = reference NO mole fraction at standard conditions

γ = second cell power of concentration ratio

α_{a2} = anodic charge transfer coefficients for the second cell

α_{c2} = cathodic charge transfer coefficients for the second cell

i_{p2}^{o} and $x_{NO,sc}^{o}$ depend on cell material and are specific to the second chamber (Ganser, Hildebrand et al. 2019). The parameters of the B-V equation can be estimated empirically (Aliramezani, Koch et al. 2019) (Yonekura, Tachikawa et al. 2011).

5.3.7 Ohmic Losses

Ohmic losses are caused by cell resistance. Ohm's law prevails in this region, and the pumping voltage is directly proportional to the pumping current. For both cells, ohmic losses are given by the following equation.

$$\eta_{o1} = i_{p1}.A_{e1}.R_1 \quad (19)$$

$$\eta_{O2} = i_{p2}.A_{e2}.R_2 \qquad (20)$$

Where,

A_{e1} = first cell electrode cross sectional area

A_{e2} = second cell electrode cross-sectional area

R_1 = first cell resistance

R_2 = second cell resistance

5.3.8 Concentration Losses

After the ohmic region, the number of molecules of the reduced species gets limited at the electrode due to insufficient diffusion of incoming gases as compared to the charge transfer speed at the electrode. This results in a constant pumping current even if the pumping voltage increases as there is no increase in the number of molecules at the cathode. The concentration losses for both the cells are given below (Haji 2011) (Etsell and Flengas 1971).

$$\eta_{c1} = \frac{RT}{F} \ln \left[\frac{i_{lim,1}}{i_{lim,1} - i_1}\right] \qquad (21)$$

$$\eta_{c2} = \frac{RT}{F} \ln \left[\frac{i_{lim,2}}{i_{lim,2} - i_2}\right] \qquad (22)$$

Where,

$i_{lim,1}$ = first chamber limiting current density

$i_{lim,2}$ = second chamber limiting current density

The values of limiting currents can be estimated from experimental I-V curves.

5.3.9 Diffusion/Mass transport model

The relation between the pumping current and the diffusion of oxygen and NOx gases from the exhaust stream to the first and second cells through the diffusion barriers can be described by combining Faraday's law and Fick's Law (Aliramezani, Koch et al. 2019) (Welty, Rorrer et al. 2020).

$$I_{P1=}i_{P1}A_{e1} = -2F\left(\frac{P}{RT}\right)D_{O_2}A_{D1}\left[\frac{x_{O2,env}-x_{O2,fc}}{L_{D1}}\right] \quad (23)$$

$$I_{P2=}i_{P2}A_{e2} = -2F\left(\frac{P}{RT}\right)D_{NO}A_{D2}\left[\frac{x_{NO,env}-x_{NO,sc}}{L_{D2}}\right] \quad (24)$$

Where,

P = pressure of exhaust gases

D_{O_2} = diffusion coefficient of O_2

D_{NO} = diffusion coefficient of NO

A_{D1} = area of first diffusion barrier

A_{D2} = area of second diffusion barrier

L_{D1}= length of first diffusion barrier

L_{D2}= length of second diffusion barrier

$x_{NO,env} = NO\ mole\ fraction\ in\ exhaust\ stream$

The diffusion coefficients depend highly on the exhaust temperature (Dietz 1982).

5.4 Results and Discussion

The parameters listed by (Aliramezani, Koch et al. 2019) are used to solve the model in Engineering Equation Solver (EES) software and successfully plot the

characteristic I-V curves for different mole fractions of both O_2 and NOx, as shown in Figures 29 and 30. It is important to note that the characteristic shape of the I-V curve for an amperometric sensor can only be achieved by including all three types of polarization. The activation loss term is responsible for the beginning of current flow at a voltage different than 0V. The Ohmic loss term is responsible for the linear increase of current with respect to voltage and, in the end, the concentration loss term starts to bend the curve horizontally. At this point, the limiting current region is reached, and the current remains constant despite increasing the voltage. The model presented in this thesis is comprehensive and can be used for parameter estimation and calibration of an amperometric sensor for required conditions. Different parameters involved in the model have their effects on the I-V curves and are discussed individually.

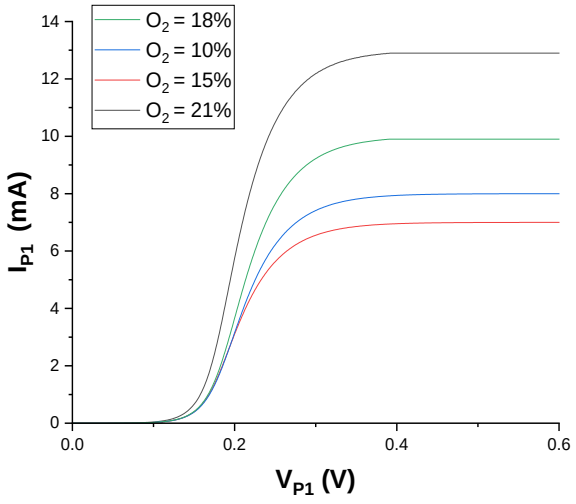

Figure 29. I-V curve for first chamber

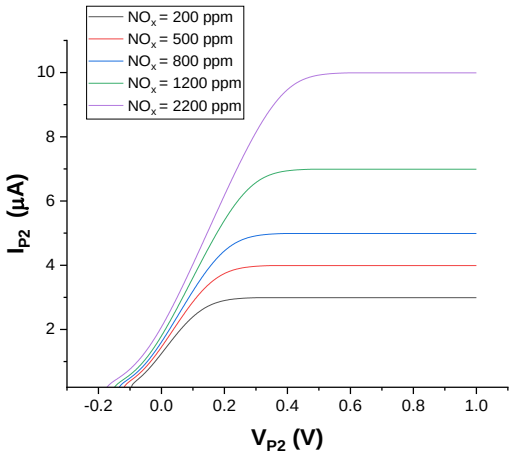

Figure 30. I-V curve for second chamber

5.4.1 Resistance

The resistance value of the sensor is responsible for the slope of the curve in the ohmic region. According to Ohm's law, increasing the resistance increases the slope of the ohmic region and it is visible after the activation polarization region, as illustrated in Figure 31.

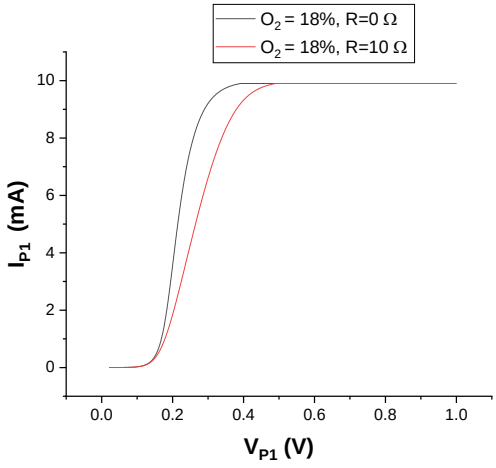

Figure 31. Effect of resistance on I-V curves

5.4.2 Temperature

The temperature of gases affects both the activation and ohmic losses, as illustrated in Figure 32. It may also affect the concentration losses, which can be proved experimentally. At higher temperatures, the tendency of the natural redox reaction to occur is higher, so more energy or pumping voltage is required to reverse it.

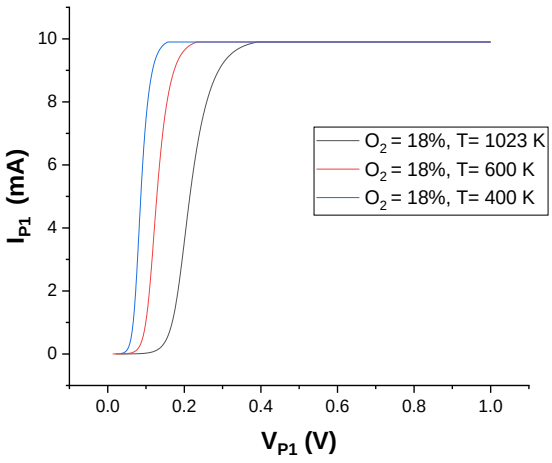

Figure 32. Effect of temperature on I-V curves

5.4.3 Limiting Current

The value of limiting current, which is to be measured experimentally, is responsible for bending the curve in the horizontal direction. It is vital to measure the correct value as choosing the wrong value can lead to an incorrect I-V curve, as shown in Figure 33. The limiting current starts affecting the I-V curve close to the limiting current region as it is associated with concentration polarization only.

5.4.4 Kinetic Parameters

Choosing a smaller value for kinetic parameters such as charge transfer coefficient or exchange current density shifts the curve to the right. A bigger value shifts it to

the left, as is evident in Figures 34 and 35. This behavior is as expected because the activation polarization parameters are only relevant in identifying a voltage where the current begins to flow and become irrelevant as soon as the ohmic region starts.

The significance of the model increases with this kind of curve shift in the context of the current research regarding NOx/O_2 sensor degradation. As the kinetic parameters are dependent on the electrode material, this curve shift from the original I-V curve identifies how much the electrode has been degraded over time. Therefore, experimental I-V curves can be taken over time to see the horizontal shift in different curves for each time stamp, indicating the electrode material degradation.

5.4.5 Diffusion Coefficient

The diffusion coefficient depends on temperature and the species of gases being diffused (Dietz 1982). As shown in Figure 36, it does not affect the activation polarization much, as the rate-determining step in the earlier part of electrode activity is not diffusion. The significance of the diffusion coefficient increases as the voltage gets closer to the limiting current region because the rate-determining step now is the diffusion.

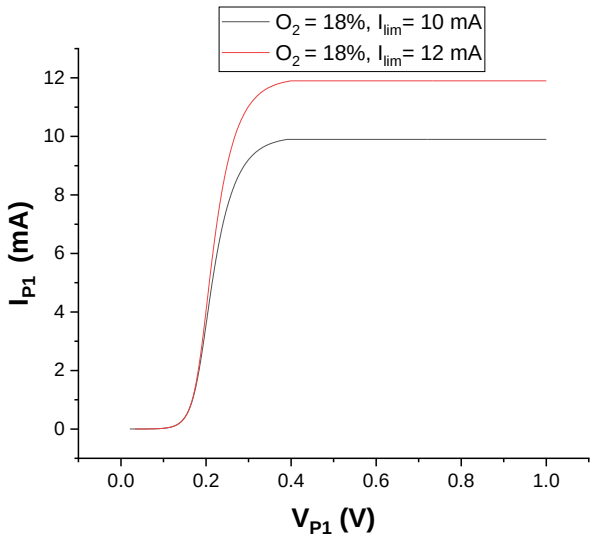

Figure 33. Effect of limiting current on I-V curves

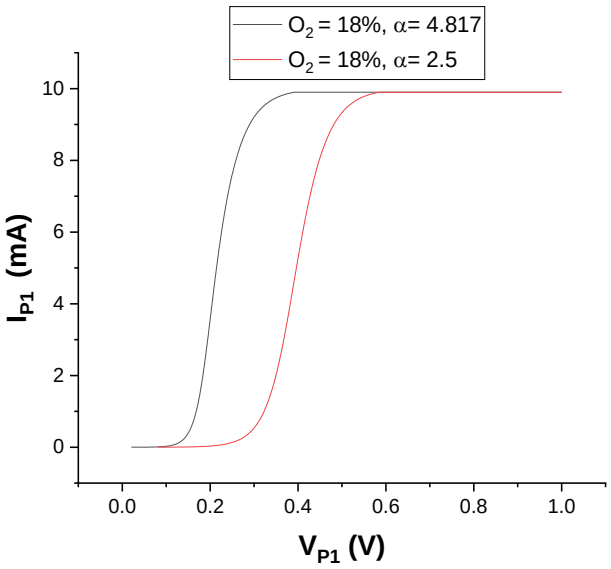

Figure 34. Effect of charge transfer coefficient of I-V curves

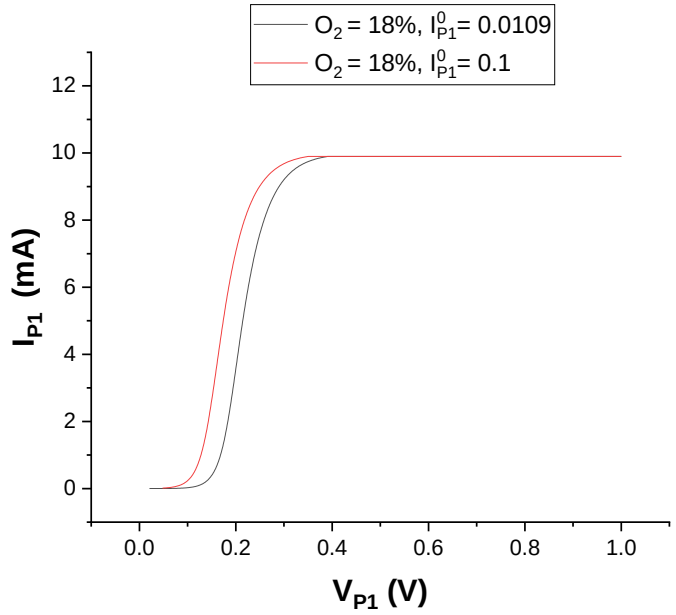

Figure 35. Effect of exchange current density at reference state on I-V curves

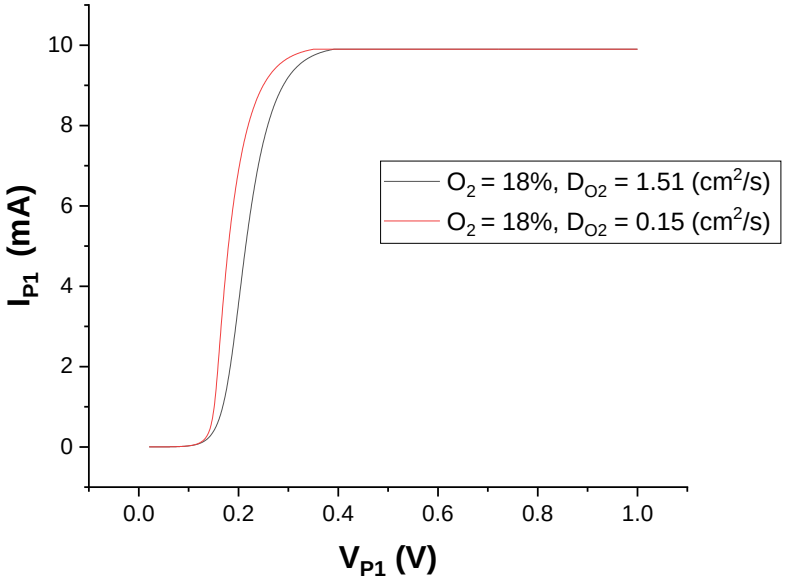

Figure 36. Effect of diffusion coefficient on I-V curves

5.5 NOx sensor Calibration

As the NOx/O_2 sensor operates on the electrochemical principle and in a very harsh environment in terms of temperature, flow rate and pollutants, it is inevitable that after a specific duration, the sensor output is affected by the electrode and diffusion barrier material deterioration. As a result, the geometric parameters, especially the kinetic parameters, are altered as they depend heavily on the condition of the electrode. Therefore, an experimental calibration method is required to accommodate for the errors in measurements. The schematic diagram of the experimental setup and the actual lab setup are shown in Figures 37 and 38 respectively.

In this experiment, a mixture containing known concentrations of the gases such as N_2, O_2, NO, NO_2, CO_2, CO and CH_4 is passed through a circulation heater and heated pipe to emulate the actual exhaust pipe. The NOx/O_2 sensor is installed in the pipe and the sensor readings are displayed on e!COCKPIT interface. A comparison is made between measured and theoretical values of O_2 and NOx. The parameters of interest here are measurement error and cross-sensitivity of NOx and O_2 to other gases present in the exhaust. Some of the results are shared in the next section.

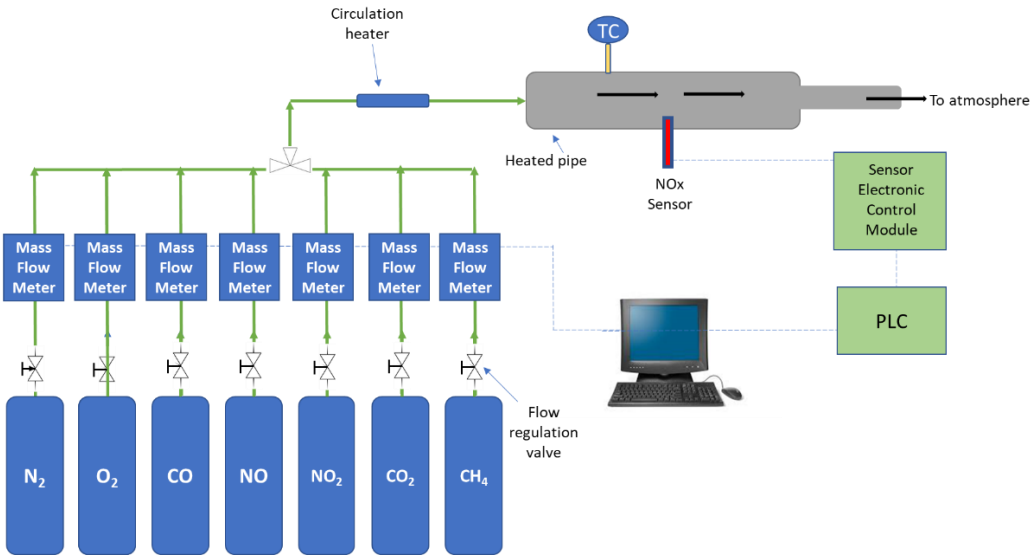

Figure 37. Schematic diagram of NOx sensor calibration experimental setup

5.5.1 Calibration Process

The calibration was started with O_2 and N_2 only. The values for theoretical O_2 concentrations are compared with the measured values and the measurement error is calculated. The range chosen for O_2 concentrations is 5-15% which is closer to the experimental values of exhaust O_2 concentrations. Moreover, the values of stack temperature and mass flow rate are also changed to see the effect of these values on the sensor measurements. The error values obtained through this calibration process will be accommodated in the PLC by introducing a new variable and adjusting the error to the original value.

Some terminologies to understand the calibration process are discussed below.

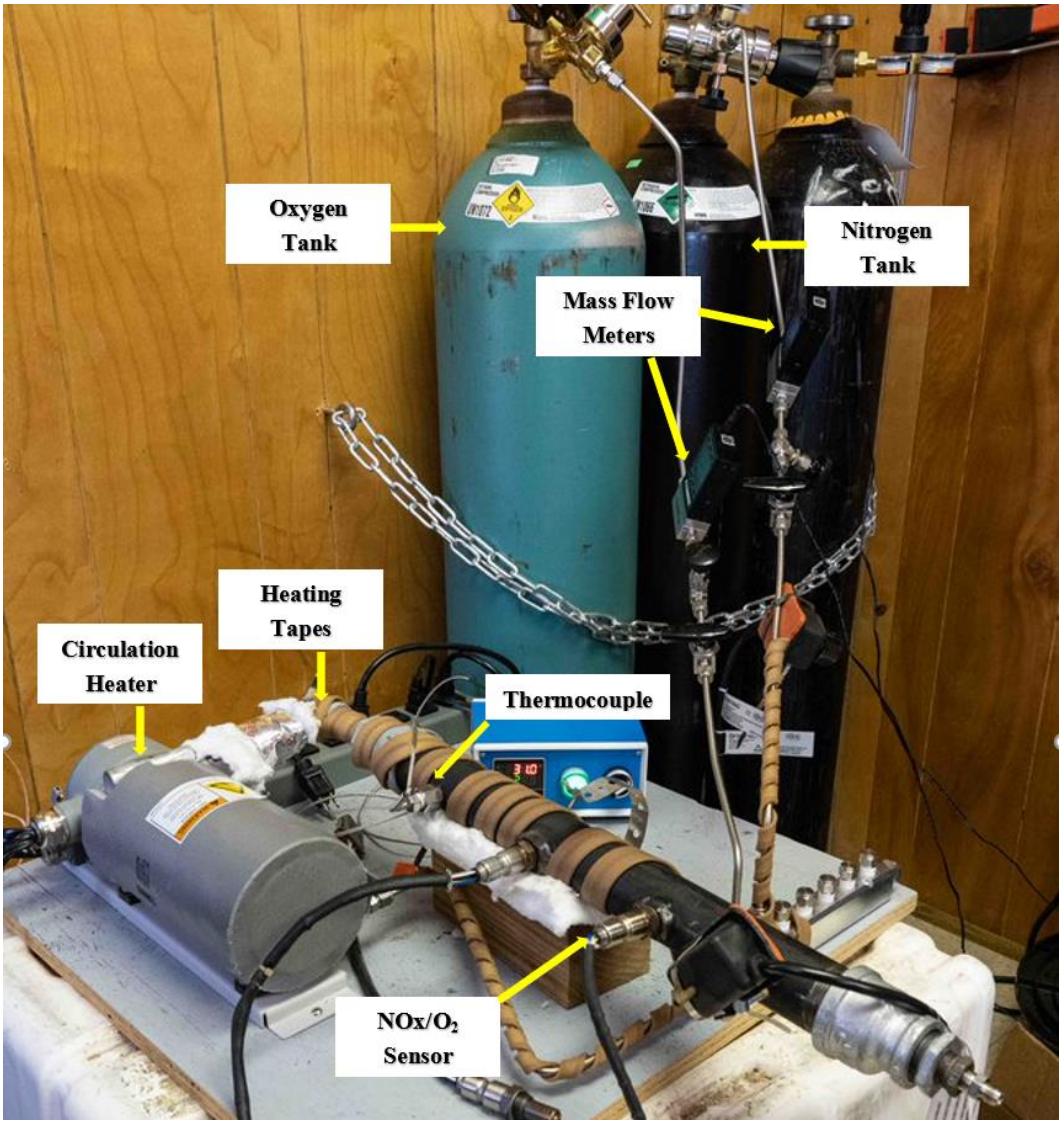

Figure 38. NOx/O_2 sensor calibration lab setup

Cross-sensitivity

The amperometric sensor is designed in a way that only the gas to be measured participates in the electrochemical process. This is achieved by choosing an electrode that is suitable for the activation energy barrier related to that particular gas. For the other gases, the activation energy is not achieved. However, in some

cases e.g., at different temperatures and higher concentrations of other gases, the electrochemical reactions for other gases such as O_2 and CO may also start. This leads to an output signal which is not entirely dependent on the gas to be measured. In fact, it would be the sum of the gas to be measured and the other gas that also got reduced. This phenomenon is referred to as the cross-sensitivity of the sensor.

Selectivity

Selectivity is the ability of the sensor to detect a target gas from an unknown mixture. It is defined as the ratio of the sensor response to a target gas to the sensor response to an interfering gas (Tonezzer, Izidoro et al. 2019). It is related to the cross-sensitivity in a way that if a sensor is more selective, it has less cross-sensitivity.

Accuracy and Uncertainty

The terms accuracy and uncertainty are closely related to each other in terms of sensor calibration. Uncertainty is given as a confidence interval to the measured value: the lesser the uncertainty, the greater the accuracy of the sensor. The following equation gives the uncertainty.

$$U_{meas} = \sqrt{{U_{inst}}^2 + {U_{gas}}^2} \qquad (25)$$

Where

U_{meas} = uncertainty from measurement

U_{inst} = uncertainty from the instrument

U_{gas} = uncertainty from the gas cylinder

Figures 39 and 40 represent O_2 calibration results at room temperature and 188°C respectively, for both the theoretical and values measured by the NOx/O_2 sensor.

For both these conditions, the mass flow rate of the mixture is kept to 11 liters per minute (LPM). As can be seen in Figures 39 and 40, the percentage error gets higher with the increasing temperature.

5.5.2 Initial Results from Calibration

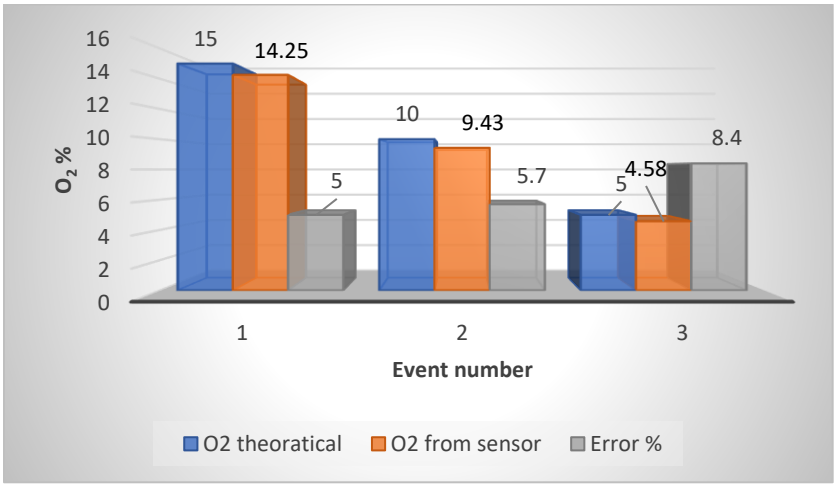

Figure 39. O_2 calibration results (room temperature, 11 LPM)

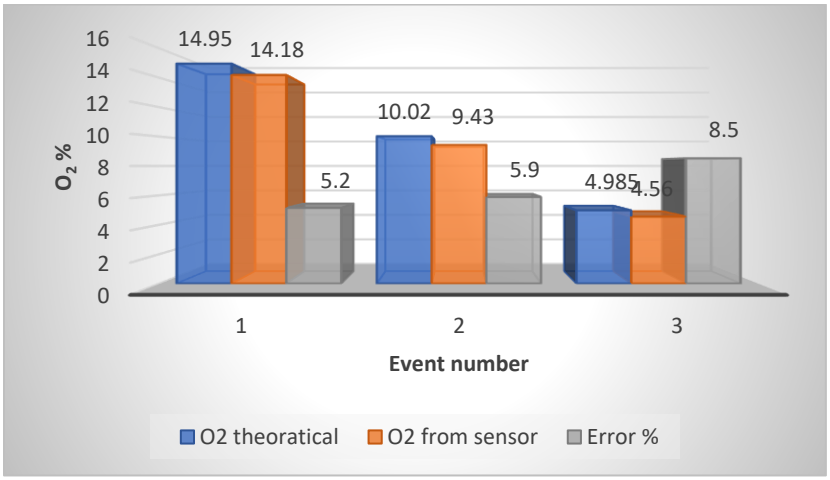

Figure 40. O_2 calibration results (188^{o}C temperature, 11 LPM)

Chapter 6

Conclusion

6.1 The Integrated System

An integrated system was investigated and its effectiveness in terms of emissions and combustion stability were experimentally investigated. The experiments were carried out for three different load conditions i.e., 40%, 60% and 75% loads. Both external and internal bypass mechanisms were tested for the integrated system. Moreover, natural gas and natural gas/propane blends were used to investigate the effectiveness of the bypass mechanism in terms of VOCs separately. The results could be interpreted in the following points.

6.1.1 40% load

- With only natural gas as fuel, CH_4, VOCs and NOx emissions were minimum at 100% bypass valve opening. CO increased with the bypass valve and were maximum at 100%. 84% and 63% reduction in CH_4 and NOx emissions was observed at 100% bypass valve opened.
- With natural gas/propane blends, same trends were observed for emissions but the reduction in VOCs was much more significant i.e., 63% reduction.
- With internal bypass using natural gas, same trends were observed for the emissions as the external bypass at 40% load.
- The combustion stability improved significantly as the bypass valve was opened and was optimum at 100% bypass valve opened. Similarly, the ITE increased by 4.2% and was maximum at 100% bypass valve opened. It shows better fuel consumption and engine performance.

6.1.2 60% load

- With only natural gas as fuel, CH_4 and VOCs emissions were minimum at 60% bypass valve opening. NOx emissions were minimum at 40% and CO were minimum at 70% bypass opening. CH_4 reduced by 68%.
- With natural gas/propane blends, CH_4, VOCs and NOx emissions were minimum at 80% bypass valve opening. At the same time, CO were minimum at 60% bypass opening. VOCs reduced by 69%.
- With internal bypass using natural gas, the CH_4, VOCs and NOx emissions reduced, but CO emissions increased.
- The ITE improves significantly as the bypass valve is opened. The ITE shows an increase of 3.8% at 60% bypass valve opening.

6.1.3 75% load

- With only natural gas as fuel, CH_4 and NOx emissions were minimum at 40% bypass valve opening. CO and VOCs changed minimally as these emissions were already very low at 75% load.
- Combustion performance improved in terms of combustion stability and ITE, but these improvements were lower at 75% load than lower loads. The ITE increased by 1.5% at 40% bypass valve opening.

As the external bypass provides more incremental control and is easily accessible during the engine's operation, it is a better option than the internal bypass. Moreover, internal bypass reduced the capability of the engine to operate at loads higher than 60%. The results are promising and show that the air management package, specifically the external bypass system, is a highly effective method to

overcome combustion instability and emissions challenges, especially at lower loads.

6.2 Amperometric NOx/O_2 sensor

A comprehensive model of an amperometric NOx/O_2 sensor was developed, capable of generating the characteristic I-V curves. The model incorporates the electrode polarization and the diffusion mechanism and is validated through I-V curves plotted through Engineering Equation Solver (EES) software. Solid-state gas sensors are cheap, reliable, easily replaceable and can be integrated into a PLC to visualize real-time measurements. This model is essential for identifying the appropriate pumping voltage for a desired range of concentrations. Moreover, the behavior of a particular sensor, its geometric and electrochemical parameters, and the durability of electrode material can be analyzed by generating the I-V curves and comparing them with experimental I-V curves.

6.3 Future Work

A machine learning model will be developed to predict the position of the bypass valve for optimum engine operations using the feedback from integrated pressure, temperature, vibration sensors and an electrochemical NOx/O_2 sensor through the PLC. Moreover, natural gas/hydrogen blends will also be investigated in terms of their effect on emissions and combustion performance. Its effect on the durability of combustion chamber material will also be studied. Moreover, an amperometric NOx/O_2 sensor will be calibrated for extremely high excess O_2 i.e., 14-15%, and a PLC setup will be developed to plot the experimental I-V curves.

References

"Overview of Greenhouse Gases." from epa.gov/ghgemissions/overview-greenhouse-gases#methane.

"U.S. Natural Gas Gross Withdrawals." from https://www.eia.gov/dnav/ng/hist/n9010us2A.htm.

(2021). "Subpart JJJJ - Standards of Performance for Stationary Spark Ignition Internal Combustion Engines." from https://www.ecfr.gov/current/title-40/chapter-I/subchapter-C/part-60/subpart-JJJJ?fbclid=IwAR1BD2mJ9QiTh2dGhOC1fXZ-NPmhz3OAVpgYiFjSDxdBKXL2v6zWDBOk350.

Akansu, S. O., Z. Dulger, N. Kahraman and T. N. Veziroğlu (2004). "Internal combustion engines fueled by natural gas—hydrogen mixtures." International journal of hydrogen energy **29**(14): 1527-1539.

Alippi, C., C. de Russis and V. Piuri (2003). "A neural-network based control solution to air-fuel ratio control for automotive fuel-injection systems." IEEE Transactions on Systems, Man, and Cybernetics, Part C (Applications and Reviews) **33**(2): 259-268.

Aliramezani, M. and C. Koch (2021). Response Characteristics of an Amperometric NOx-O2 Sensor at Non diffusion-Rate-Determining Conditions, SAE Technical Paper.

Aliramezani, M., C. R. Koch, R. E. Hayes and R. Patrick (2017). "Amperometric solid electrolyte NOx sensors–the effect of temperature and diffusion mechanisms." Solid State Ionics **313**: 7-13.

Aliramezani, M., C. R. Koch, M. Secanell, R. E. Hayes and R. Patrick (2019). "An electrochemical model of an amperometric NOx sensor." Sensors and Actuators B: Chemical **290**: 302-311.

Amphlett, J. C., R. M. Baumert, R. F. Mann, B. A. Peppley, P. R. Roberge and T. J. Harris (1995). "Performance modeling of the Ballard Mark IV solid polymer electrolyte fuel cell: I. Mechanistic model development." Journal of the Electrochemical Society **142**(1): 1.

Andwari, A. M., A. A. Aziz, M. F. M. Said, V. Esfahanian, Z. A. Latiff and S. N. M. Said (2017). "Effect of internal and external EGR on cyclic variability and emissions of a spark ignition two-stroke cycle gasoline engine." Journal of mechanical engineering and sciences **11**(4): 3004.

Anjum, R., I. Khan, A. Yar and A. I. Bhatti (2017). Air-to-fuel ratio control of gasoline engines using smooth sliding mode algorithm. 2017 13th international conference on emerging technologies (ICET), IEEE.

Aslam, M., H. Masjuki, M. Kalam, H. Abdesselam, T. Mahlia and M. Amalina (2006). "An experimental investigation of CNG as an alternative fuel for a retrofitted gasoline vehicle." Fuel **85**(5-6): 717-724.

Baukal Jr, C. E. (2012). The john zink hamworthy combustion handbook: Volume 1-Fundamentals, CRC press.

Benammar, M. (1994). "Techniques for measurement of oxygen and air-to-fuel ratio using zirconia sensors. A review." Measurement Science and Technology **5**(7): 757.

Betteridge, W. J. (2006). NOx Sensor for Direct Injection Emission Control, Electricore, Inc.

Chang, C.-F., N. P. Fekete, A. Amstutz and J. Powell (1995). "Air-fuel ratio control in spark-ignition engines using estimation theory." IEEE Transactions on Control Systems Technology **3**(1): 22-31.

Chapman, K. S. (2004). Cost-Effective Reciprocating Engine Emissions Control and Monitoring for E&P Field and Gathering Engines. United States**:** Medium: ED.

Chapman, K. S. and S. R. Nuss-Warren (2007). Cost-Effective Reciprocating Engine Emissions Control and Monitoring for E&P Field and Gathering Engines, Kansas State Univ., Manhattan, KS (United States).

Chen, H., J. He and X. Zhong (2019). "Engine combustion and emission fuelled with natural gas: a review." Journal of the Energy Institute **92**(4): 1123-1136.

Coillard, V., L. Juste, C. Lucat and F. Ménil (2000). "Nitrogen-monoxide sensing with a commercial zirconia lambda gauge biased in amperometric mode." Measurement Science and Technology **11**(3): 212.

Collings, N., K. Hegarty and T. Ramsander (2012). "Steady-state modelling of the universal exhaust gas oxygen (UEGO) sensor." Measurement Science and Technology **23**(8): 085108.

Cooper, J., P. Balcombe and A. Hawkes (2021). "The quantification of methane emissions and assessment of emissions data for the largest natural gas supply chains." Journal of Cleaner Production **320**: 128856.

da Costa, R. B. R., J. J. Hernandez, A. F. Teixeira, N. A. D. Netto, R. M. Valle, V. R. Roso and C. J. Coronado (2019). "Combustion, performance and emission analysis of a natural gas-hydrous ethanol dual-fuel spark ignition engine with internal exhaust gas recirculation." Energy Conversion and Management **195**: 1187-1198.

del Olmo, D., M. Pavelka and J. Kosek (2021). "Open-Circuit Voltage Comes from Non-Equilibrium Thermodynamics." Journal of Non-Equilibrium Thermodynamics **46**(1): 91-108.

Dey, S. and G. C. Dhal (2019). "Materials progress in the control of CO and CO2 emission at ambient conditions: an overview." Materials Science for Energy Technologies **2**(3): 607-623.

Dietz, H. (1982). "Gas-diffusion-controlled solid-electrolyte oxygen sensors." Solid State Ionics **6**(2): 175-183.

Docquier, N. and S. Candel (2002). "Combustion control and sensors: a review." Progress in energy and combustion science **28**(2): 107-150.

Engh, G. T. and S. Wallman (1977). "Development of the Volvo Lambda-sond system." SAE Transactions: 1393-1408.

Etsell, T. and S. Flengas (1971). "Overpotential behavior of stabilized zirconia solid electrolyte fuel cells." Journal of the Electrochemical Society **118**(12): 1890.

Feiner, A.-S. and A. McEvoy (1994). "The nernst equation." Journal of chemical education **71**(6): 493.

Fernández-Solis, C. D., A. Vimalanandan, A. Altin, J. S. Mondragón-Ochoa, K. Kreth, P. Keil and A. Erbe (2016). Fundamentals of electrochemistry, corrosion and corrosion protection. Soft Matter at Aqueous Interfaces, Springer**:** 29-70.

Ganser, M., F. E. Hildebrand, M. Klinsmann, M. Hanauer, M. Kamlah and R. M. McMeeking (2019). "An extended formulation of butler-volmer electrochemical reaction kinetics including the influence of mechanics." Journal of The Electrochemical Society **166**(4): H167.

Gao, J., G. Tian, C. Ma, S. Xing and L. Huang (2021). "Three-dimensional numerical simulations on the effect of ignition timing on combustion characteristics, nitrogen oxides emissions, and energy loss of a hydrogen fuelled opposed rotary piston engine over wide open throttle conditions." Fuel **288**: 119722.

Gatowski, J., E. N. Balles, K. M. Chun, F. Nelson, J. Ekchian and J. B. Heywood (1984). "Heat release analysis of engine pressure data." SAE transactions: 961-977.

Grizzle, J. W., K. L. Dobbins and J. A. Cook (1991). "Individual cylinder air-fuel ratio control with a single EGO sensor." IEEE Transactions on vehicular technology **40**(1): 280-286.

Gubba, S. R., B. Tamma, P. Kazempoor, T. J. Hurley, M. A. Patterson and G. Hartman (2021). "A novel air management system for a large bore two-stroke naturally aspirated gas engine to reduce emissions." International Journal of Engine Research **22(**2): 364-374.

Haji, S. (2011). "Analytical modeling of PEM fuel cell i–V curve." Renewable Energy **36**(2): 451-458.

Hassan, H. A., M. Hartless, P. Jha and P. Kazempoor (2022). Integrated System to Reduce Emissions from Natural Gas-Fired Reciprocating Engines—Performance Assessment of Amperometric NOx/O2 Sensors, SAE Technical Paper.

Heywood, J. B. (2018). Internal combustion engine fundamentals, McGraw-Hill Education.

Hillier, V. A. W. and P. Coombes (2004). Hillier's fundamentals of motor vehicle technology, Nelson Thornes.

Hoard, J. and L. Rehagen (1997). Relating subjective idle quality to engine combustion, SAE Technical Paper.

Ishibashi, Y. and M. Asai (1996). "Improving the exhaust emissions of two-stroke engines by applying the activated radical combustion." SAE transactions: 982-992.

Javed, U., K. P. Ramaiyan, C. R. Kreller, E. L. Brosha, R. Mukundan and A. V. Morozov (2018). "Using sensor arrays to decode NOx/NH3/C3H8 gas mixtures for automotive exhaust monitoring." Sensors and Actuators B: Chemical **264**: 110-118.

Jeeragal, R. and K. Subramanian (2019). "Experimental Investigation for NO x Emission Reduction in Hydrogen Fueled Spark Ignition Engine Using Spark Timing Retardation, Exhaust Gas Recirculation and Water Injection Techniques." Journal of Thermal Science **28**(4): 789-800.

Karim, G., I. Wierzba and Y. Al-Alousi (1996). "Methane-hydrogen mixtures as fuels." International Journal of Hydrogen Energy **21**(7): 625-631.

Keith Hohn, S. R. N.-W. (2011). Final Report: Cost-Effective Reciprocating Engine Emissions Control and Monitoring for E&P Field and Gathering Engines D. o. Energy. Kansas State University, National Gas Machinery Laboratory, 245 Levee Drive, Manhattan, KS 66502.

Kojima, M., C. Brandon and J. Shah (2000). Improving urban air quality in South Asia by reducing emissions from two-stroke engine vehicles, World Bank Washington, DC.

Korakianitis, T., A. Namasivayam and R. Crookes (2011). "Natural-gas fueled spark-ignition (SI) and compression-ignition (CI) engine performance and emissions." Progress in energy and combustion science **37**(1): 89-112.

Lauber, J., T.-M. Guerra and M. Dambrine (2011). "Air-fuel ratio control in a gasoline engine." International Journal of Systems Science **42**(2): 277-286.

Lefrou, C., P. Fabry and J.-C. Poignet (2012). Electrochemistry: the basics, with examples, Springer Science & Business Media.

Li, L. Q. and L. Tang (2012). The Amperometric NOx Sensors' Electrode Polarization and its Effect on the Offset. Advanced Materials Research, Trans Tech Publ.

Li, Z., J. Li, Q. Zhou, Y. Zhang and H. Xu (2019). "Intelligent air/fuel ratio control strategy with a PI-like fuzzy knowledge–based controller for gasoline direct injection engines." Proceedings of the Institution of Mechanical Engineers, Part D: Journal of Automobile Engineering **233**(8): 2161-2173.

Ma, F., S. Li, J. Zhao, Z. Qi, J. Deng, N. Naeve, Y. He and S. Zhao (2012). "Effect of compression ratio and spark timing on the power performance and combustion characteristics of an HCNG engine." International journal of hydrogen energy **37**(23): 18486-18491.

Ma, F., Y. Wang, H. Liu, Y. Li, J. Wang and S. Zhao (2007). "Experimental study on thermal efficiency and emission characteristics of a lean burn hydrogen enriched natural gas engine." International Journal of Hydrogen Energy **32**(18): 5067-5075.

Mann, R. F., J. C. Amphlett, M. A. Hooper, H. M. Jensen, B. A. Peppley and P. R. Roberge (2000). "Development and application of a generalised steady-state electrochemical model for a PEM fuel cell." Journal of power sources **86**(1-2): 173-180.

Menil, F., V. Coillard and C. Lucat (2000). "Critical review of nitrogen monoxide sensors for exhaust gases of lean burn engines." Sensors and Actuators B: Chemical **67**(1-2): 1-23.

Minato, A., T. Tanaka and T. Nishimura (2005). "Investigation of premixed lean diesel combustion with ultra high pressure injection." SAE transactions: 756-764.

Moos, R. (2005). "A brief overview on automotive exhaust gas sensors based on electroceramics." International Journal of Applied Ceramic Technology **2**(5): 401-413.

Moseley, P. (1997). "Solid state gas sensors." Measurement Science and technology **8**(3): 223.

Noren, D. and M. A. Hoffman (2005). "Clarifying the Butler–Volmer equation and related approximations for calculating activation losses in solid oxide fuel cell models." Journal of Power Sources **152**: 175-181.

Ono, M., K. Shimanoe, N. Miura and N. Yamazoe (2000). "Amperometric sensor based on NASICON and NO oxidation catalysts for detection of total NOx in atmospheric environment." Solid State Ionics **136**: 583-588.

Pace, S. and G. G. Zhu (2010). "Air-to-fuel and dual-fuel ratio control of an internal combustion engine." SAE International Journal of Engines **2**(2): 245-253.

Pham, A. Q. and R. S. Glass (1997). "Characteristics of the amperometric oxygen sensor." Journal of the Electrochemical Society **144**(11): 3929.

Ren, Y., D. Lou, P. Tan, Y. Zhang and X. Sun (2021). "Emission reduction characteristics of after-treatment system on natural gas engine: Effects of platinum group metal loadings and ratios." Journal of Cleaner Production **298**: 126833.

Riegel, J., H. Neumann and H.-M. Wiedenmann (2002). "Exhaust gas sensors for automotive emission control." Solid State Ionics **152**: 783-800.

Sekar, M., T. Praveenkumar, V. Dhinakaran, P. Gunasekar and A. Pugazhendhi (2021). "Combustion and emission characteristics of diesel engine fueled with nanocatalyst and pyrolysis oil produced from the solid plastic waste using screw reactor." Journal of Cleaner Production **318**: 128551.

Selamet, A., S. Rupal, Y. He and P. Keller (2004). An experimental study on the effect of intake primary runner blockages on combustion and emissions in SI engines under part-load conditions, SAE Technical Paper.

Sevik, J., M. Pamminger, T. Wallner, R. Scarcelli, R. Reese, A. Iqbal, B. Boyer, S. Wooldridge, C. Hall and S. Miers (2016). "Performance, efficiency and emissions assessment of natural gas direct injection compared to gasoline and natural gas port-fuel injection in an automotive engine." SAE International Journal of Engines **9**(2): 1130-1142.

Sharma, A. K., K. Ahmed and E. Birgersson (2018). "Nernst voltage losses in planar fuel cells caused by changes in chemical composition: Effects of operating parameters." Ionics **24**(7): 2047-2054.

T. J. Truex , R. A. Searles , D. C. Sun , Johnson Matthey (1992). "Catalysts for Nitrogen Oxides Control under Lean Burn Conditions." Platinum Metals Rev., **36** (1)

Thurnheer, T., P. Soltic and P. D. Eggenschwiler (2009). "SI engine fuelled with gasoline, methane and methane/hydrogen blends: heat release and loss analysis." International journal of hydrogen energy **34**(5): 2494-2503.

Tonezzer, M., S. C. Izidoro, J. Moraes and L. T. T. Dang (2019). "Improved gas selectivity based on carbon modified SnO2 nanowires." Frontiers in Materials: 277.

Toof, J. (1986). "A model for the prediction of thermal, prompt, and fuel NOx emissions from combustion turbines."

Wang, J., Z. Huang, Y. Fang, B. Liu, K. Zeng, H. Miao and D. Jiang (2007). "Combustion behaviors of a direct-injection engine operating on various fractions of natural gas–hydrogen blends." International Journal of Hydrogen Energy **32**(15): 3555-3564.

Wei, H., T. Zhu, G. Shu, L. Tan and Y. Wang (2012). "Gasoline engine exhaust gas recirculation–A review." Applied energy **99**: 534-544.

Welty, J., G. L. Rorrer and D. G. Foster (2020). Fundamentals of momentum, heat, and mass transfer, John Wiley & Sons.

Yang, W., M. Yang, H. Wen and Y. Jiao (2018). "Global Warming Potential of CH4 uptake and N2O emissions in saline–alkaline soils." Atmospheric Environment **191**: 172-180.

Yonekura, T., Y. Tachikawa, T. Yoshizumi, Y. Shiratori, K. Ito and K. Sasaki (2011). "Exchange current density of solid oxide fuel cell electrodes." ECS Transactions **35**(1): 1007.

Yousefi, A., A. Gharehghani and M. Birouk (2015). "Comparison study on combustion characteristics and emissions of a homogeneous charge compression ignition (HCCI) engine with and without pre-combustion chamber." Energy Conversion and Management **100**: 232-241.

Zhang, Y., D. Davis and M. J. Brear (2022). "The role of hydrogen in decarbonizing a coupled energy system." Journal of Cleaner Production **346**: 131082.

Zhao, F. and A. V. Virkar (2005). "Dependence of polarization in anode-supported solid oxide fuel cells on various cell parameters." Journal of power sources **141**(1): 79-95.